BRNO UNIVERSITY OF TECHNOLOGY

Faculty of Mechanical Engineering

MASTER'S THESIS

Brno, 2021   Mgr. Peter Kepič

BRNO UNIVERSITY OF TECHNOLOGY

FACULTY OF MECHANICAL ENGINEERING
FAKULTA STROJNÍHO INŽENÝRSTVÍ

INSTITUTE OF PHYSICAL ENGINEERING
ÚSTAV FYZIKÁLNÍHO INŽENÝRSTVÍ

DESIGN AND FABRICATION OF TUNABLE DIELECTRIC METASURFACES FOR VISIBLE AND INFRARED WAVELENGTHS
NÁVRH A VÝROBA LADITELNÝCH DIELEKTRICKÝCH METAPOVRCHŮ PRO VIDITELNÉ A INFRAČERVENÉ VLNOVÉ DÉLKY

MASTER'S THESIS
DIPLOMOVÁ PRÁCE

AUTHOR   Mgr. Peter Kepič
AUTOR PRÁCE

SUPERVISOR   Ing. Filip Ligmajer, Ph.D.
VEDOUCÍ PRÁCE

BRNO 2021

Assignment Master's Thesis

Institut:	Institute of Physical Engineering
Student:	**Mgr. Peter Kepič**
Degree programm:	Physical Engineering and Nanotechnology
Branch:	no specialisation
Supervisor:	**Ing. Filip Ligmajer, Ph.D.**
Academic year:	2020/21

As provided for by the Act No. 111/98 Coll. on higher education institutions and the BUT Study and Examination Regulations, the director of the Institute hereby assigns the following topic of Master's Thesis:

Design and fabrication of tunable dielectric metasurfaces for visible and infrared wavelengths

Brief Description:

Metasurfaces are artificial nanostructured surfaces, which can act as a whole range of conventional and special optical components. This diploma thesis should deal with metasurfaces made of vanadium dioxide (VO2), which is a unique material exhibiting a phase change from insulator to metal at easily reachable temperature. VO2 thus brings two very desirable properties to the field of metasurfaces: switchability and tunability. Within the diploma project, VO2 nanostructures will be fabricated and these potential building blocks of tunable metasurfaces will be then investigated using experiments and simulations. The acquired knowledge will be utilized for design and production of a tunable VO2 metasurface. The ultimate goal is then to demonstrate optical control over an optical component, which is one of the key capabilities for future applications of tunable metasurfaces.

Master's Thesis goals:

1. Fabrication of vanadium dioxide nanostructures. Characterization of their optical properties in both material phases.
2. Analyzing the potential of the vanadium dioxide nanostructures for optical tunability using visible light.
3. Fabrication of a prototypical metasurface (e.g. metalens) made of vanadium dioxide building blocks.

Recommended bibliography:

LIGMAJER, Filip, 2018. Advanced plasmonic materials for metasurfaces and photochemistry. Brno. Dizertační práce. VUT v Brně.

APPAVOO, Kannatassen, Dang Yuan LEI, Yannick SONNEFRAUD, Bin WANG, Sokrates T. PANTELIDES, Stefan A. MAIER a Richard F. HAGLUND, 2012. Role of Defects in the Phase Transition of VO 2 Nanoparticles Probed by Plasmon Resonance Spectroscopy. Nano Letters. 12(2), 780-786. ISSN 1530-6984. Dostupné z: doi:10.1021/nl203782y

BUTAKOV, Nikita A., Ilya VALMIANSKI, Tomer LEWI, et al., 2017. Switchable Plasmonic–Dielectric Resonators with Metal–Insulator Transitions. ACS Photonics [online]. 5(2), 371-377 [cit. 2020-10-22]. ISSN 2330-4022. Dostupné z: doi:10.1021/acsphotonics.7b00334

Deadline for submission Master's Thesis is given by the Schedule of the Academic year 2020/21

In Brno,

L. S.

prof. RNDr. Tomáš Šikola, CSc.
Director of the Institute

doc. Ing. Jaroslav Katolický, Ph.D.
FME dean

Abstract

Metasurfaces are nanostructured surfaces that can be fabricated to specifically manipulate the propagation of light. They represent a revolution in ultrathin optics and nanophotonic circuits. Adding tunable dielectric materials into metasurfaces' designs enable them to actively control their optical properties after being fabricated. Vanadium dioxide (VO_2) is one of the most promising materials that could provide such tunability due to its phase-transition at temperatures around $67\,°C$. Being able to gradually induce VO_2 phase-transition also optically, with a light beam being focused to a few hundreds of nanometers, tunable metasurfaces based on VO_2 could be gradually tuned with nanoscale resolution. Here, we demonstrate a full transmission phase and amplitude investigation of VO_2 nanostructures for metasurfaces operating in the visible part of the electromagnetic spectrum. The investigation of VO_2 nanostructures (metasurface building blocks) is mostly done by simulations, which are later supported by experimental results. Moreover, VO_2 nanostructures exhibit Mie resonances that are subsequently utilized for a gradually tunable metasurface in the visible. Besides thermal tuning, the fabricated metasurface is also tuned optically, proving the possibility of gradual optical tuning.

Keywords

Abstrakt

Metapovrchy sú nanoštruktúrované povrchy vytvorené za účelom špecifického ovládania propagácie svetla. Predstavujú revolúciu v oblastiach ultratenkých optických prvkov a nanofotonických obvodov. Zakomponovaním laditeľných dielektrických materiálov do metapovrchov sa otvára možnosť aktívne ovládať ich optické vlastnosti aj po tom, čo boli vyrobené. Oxid vanadičitý (VO_2) takéto ladenie umožňuje vďaka svojej fázovej premene už pri teplote okolo 67 °C a preto sa radí k najsľubnejším z laditeľných dielektrických materiálov. Nakoľko je možné postupnú fázovú premenu vo VO_2 vybudiť opticky a lúč svetla je možné fokusovať do stopy s veľkosťou pár stoviek nanometrov, laditeľné metapovrchy obsahujúce VO_2 by mohli byť ladené postupne a dokonca s nanometrovým rozlíšením. V tejto práci skúmame fázu a amplitúdu svetla po prechode VO_2 nanoštruktúrami usporiadanými do metapovrchu navrhnutého pre viditeľnú zložku elektromagnetického žiarenia. Výskum fáze a amplitúdy je založený na numerických simuláciách VO_2 nanoštruktúr (stavebných kameňov metapovrchov), ktoré sú následne overené experimentálnymi výsledkami. VO_2 nanoštruktúry vykazujú taktiež Mieho dielektrické rezonancie, ktoré sú v závere tejto práce využité v postupne laditeľnom metapovrchu fungujúcom vo viditeľnej oblasti. Okrem termálneho ladenia je možné vyrobený metapovrch ovládať taktiež opticky, čo dokazuje možnosť postupného ladenia na nanometrových rozmeroch.

Klíčová slova

metapovrch, laditľný metapovrch, oxid vanadičitý, Mieho rezonancia

Prehlasujem, že som predloženú diplomovú prácu s názvom "Návrh a výroba laditeľných dielektrických metapovrchů pro viditelné a infračervené vlnové délky" vypracoval samostatne pod vedením Ing. Filipa Ligmajera, Ph.D, a že všetky podklady, z ktorých som čerpal, uvádzam v priloženom zozname použitej literatúry.

Mgr. Peter Kepič

Contents

Introduction

Diffracting entangled photons to determine their prior polarization or encoding hologram information into the angular momentum of a photon — tasks that can be hardly achieved with conventional optical components — can be nowadays performed with metasurfaces. These ultrathin surfaces made of nanostructures, which can manipulate propagation of light on demand, make use of many years of research in the field of nanophotonics. In case the nanostructures themselves are made of active materials which optical properties can be altered after fabrication, the metasurface can be upgraded into a tunable one. The most promising materials introducing tunability are phase-change materials, out of which germanium–antimony–telluride (GST) and vanadium dioxide (VO_2) get the biggest attention. While advantage of GST lies in its nonvolatile structural transition from amorphous to crystalline form, VO_2 is mostly sought after for its volatile transition, occurring already around $67\,°C$ and withstanding millions of switching cycles without degradation. Another advantage of VO_2 is its large index contrast in the visible range ($\Delta n \approx 1$) that vastly exceeds those of other phase-change materials. Because of these advantages, the main goal of this thesis is to examine the potential of pure VO_2 nanostructures in metasurfaces that operate in the visible region.

Chapter 1 starts with a description of the physics of metasurfaces, which are investigated on both microscopic and macroscopic levels. Through the process of metasurface design we look closer on the state-of-the-art applications. Lastly, we introduce various platforms for tunable metasurfaces, while focusing mainly on phase-change materials.

Chapter 2 is devoted to VO_2, specifically to the nature of its transition, techniques used for inducing this transition and methods used for its deposition. Out of various quality factors for nanophotonic applications, modulation of VO_2 refractive index is then established as the best fitted one. Using the optical figure of merit taking into account losses and tunability magnitudes, we study the relationship between the optical magnitude modulation and structural quality of VO_2. After this investigation, we conclude the chapter with an overview of state-of-the-art applications of VO_2 in metasurfaces.

In chapter 3 we introduce fabrication and characterization methods used within this work. Specifically, we describe two fabrication methods — electron beam evaporation and electron beam lithography — that are used for thin film deposition and fabrication of nanostructures, respectively. Then, we describe two characterization methods — spectroscopic ellipsometry and coherence-controlled holographic microscopy — that are used for dielectric function retrieval, and amplitude and phase measurement, respectively.

Chapter 4 summarizes all obtained results that are divided into 3 parts: In the first part we describe the process of VO_2 thin film optimization. The dielectric function of the optimized VO_2 is then used in the second part for simulations of transmission phase and amplitude of metasurface VO_2 nanocylinders. Simulations are partially verified by measurements of fabricated nanostructures. In the third part, we demonstrate utilization of dielectric Mie resonances in VO_2 nanostructures for a transmission filter metasurface. Using this transmission metasurface we prove the possibility of both thermal and optical gradual tuning of the optical function, which confirms the large potential of VO_2 in the domain of tunable metasurfaces.

1.   Metasurfaces

From the first use of a burning glass in Ancient Greece [1] to nowaday's highly efficient and multifunctional bulk optical components, the humankind has always striven to control the propagation of light. While being used for computation, recording or telecommunication, optical components have become an inseparable part of everyone's life. Metasurfaces represent the next step in the development of optics, as these ultra-thin nanostructured surfaces can act as all sorts of optical components. This fact is supported not only by a growing number of scientific publications [2], but also by their commercial implementation in the recently established business called Metalenz [3].

Such growing interest in metasurfaces is also what led us to this thesis and why the first chapter is devoted to the description of metasurfaces. In the first section, a typical metasurface is described on a microscopic level, where physics behind the light control is explained. In the second part, design of metasurfaces and state of the art applications are outlined. Lastly, as metasurfaces can be improved by tunability and this thesis is focused on this topic, tunable metasurfaces receive more attention at the end of this chapter.

1.1   Physics of metasurfaces

To fully understand the metasurface theory, let us first start with a lens development. Imagine a regular bulk refractive lens that is illuminated by a planar electromagnetic wave. Assuming this wave is fully described by its amplitude, phase and polarization, a focusing property of this lens is achieved by the hyperbolically varying material thickness that creates the specific phase shift at each infinitesimally small annulus. Taking out the amount of material that introduces a full-wave phase shift (as illustrated in Figure 1.1), the lens can be reduced into so-called Fresnel lens, proposed by Augustin-Jean Fresnel in 1821 [4]. Even though this concept has its drawbacks in form of abberations and complicated fabrication, it is still widely used in lighthouses or searchlights nowadays. The Fresnel lens is based on general diffraction theory, de-
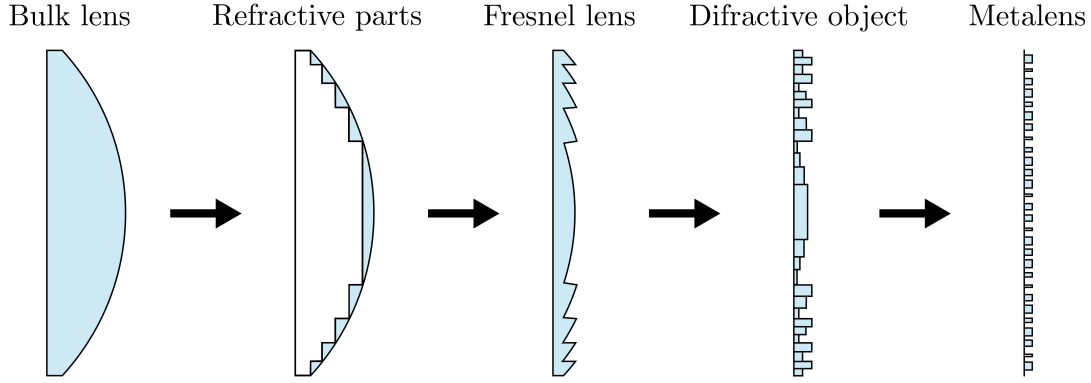
Figure 1.1: Scheme describing evolution from bulk optical components into metasurfaces. Adapted from [6].

scribed by the Huygens-Fresnel principle [5]. In this theory, the lens can be replaced by a diffractive object that is made of a thickness-varying surface. This surface provides the desired propagation-phase shift (Figure 1.1). From such diffractive object, there is only one more step to obtain the metalens or metasurface. While diffractive objects represent thickness-varying films, metasurfaces are composed of specifically fabricated nanostructures that have in most cases fixed height and spacing, but varying dimensions or shapes. The phase shift in this case is produced by altering the size or shape of each nanostructure, which is then often called a building block. These nanostructured building blocks form the metasurface.

The physics of this building block phase shift lies in the propagation of light through the block (propagation-phase) or in rotation of the specific block (geometrical phase). In the first case, the propagation-phase in metasurfaces can be derived from the propagation-phase shift $\phi_{\mathrm{p}}(x,y)$ introduced by a spatially-varying thickness $t(x,y)$ in diffractive objects

$$\phi_{\mathrm{p}}(x,y) = \frac{2\pi}{\lambda}(n-1)\,t(x,y),\tag{1.1}$$

where λ is the wavelength in vacuum, n the refractive index of the building block and 1 is the refractive index of a surrounding medium (in this case air). The requirement of spatially-varying thickness is the main limit of diffractive objects, as they are difficult to fabricate [7]. The easier way is to fix the height and try to spatially vary the refractive index. This can be obtained by replacing diffractive surfaces with small separate building blocks and therefore changing equation 1.1 into [8]

$$\phi_{\mathrm{p}}(x,y) \approx \frac{2\pi}{\lambda}(n_{\mathrm{eff}}(x,y)-1)\,t,\tag{1.2}$$

where n_{eff} is now an effective refractive index. This effective index is sensitive to the

shape or the lateral size of the building blocks due to one of these processes: plasmonic resonances in metal structures [9], gap surface plasmons in metal–insulator–metal structures [10], Mie resonances in high-index dielectric structures [11], or multiple modes in high aspect ratio dielectric structures [12].

When properly excited, metal structures with a dielectric interface can exhibit the localized surface plasmon resonance. This resonance is highly dependent on the lateral size, shape and configuration of these structures [13]. Spectrally shifting the resonance results in the change of structure's effective refractive index [14]. Advantages of incorporating such building blocks into metasurfaces are no need for high aspect ratio structures and well-developed fabrication. Besides these advantages, metallic structures also exhibit a large absorption coefficient in the visible part of the spectrum. While this absorption might be useful for absorbing or thermally-radiating metasurfaces [9], it significantly limits plasmonic metasurfaces for beam shaping or focusing [2].

Based also on plasmonic principle, gap surface plasmon metasurfaces are constructed by adding a dielectric spacer between a metallic substrate and a plasmonic nano-structure. In the gap plasmon resonance, strong near-field coupling between the metallic nanoantenna and the metal substrate is formed, creating a strong magnetic field, by which a 2π phase shift can be achieved [15]. It is important to mention that due to plasmon modes confined within the spacer, the phase shift is controlled not only by the nanoantenna size, but also by the spacer thickness [16]. Using the gap-surface plasmon principle, the efficiency in the visible goes up to $80\,\%$ [17], but due to the metal substrate, the metasurface is limited to reflective applications.

Mie resonances in high-index dielectric structures have the similar effect on n_{eff} as plasmonic resonances, but the resonance origin is different. Specifically, the electron current in metals is replaced by the displacement current in high refractive index dielectrics [18]. This results in excitation of electric and magnetic multipoles, which have very unique applications. One such application is so-called Huygens metasurface, which exhibits a significantly reduced back-scattering response due to spectrally over-lapping electric and magnetic multipoles [19]. Another extraordinary application can be super-localization nanoscopy with a non-radiative anapole mode, in which the electric dipole interferes destructively with a toroidal mode, while enhancing local magnetic field [20]. These and many other applications seem to make Mie resonant dielectric building blocks highly perspective for metasurfaces, however a very recent study revealed a fundamental limit that arises from short and long-range interactions between Mie resonant structures in arrays [21].

The phase modulation in high aspect ratio dielectric structures is also formed by the dielectric resonant modes as in Mie structures. Nonetheless, due to their height, they often support many spectrally overlapping modes. This way, these high aspect ratio structures are no longer characterized by they resonances, but as tiny waveguides that can be described by the waveguide theory [22]. What makes them one of the most used structures for metasurfaces are short range interactions [21] and very low absorption that results in high transmission efficiency [23]. The only problematic aspect is the height of the building blocks, which makes fabrication more complicated.

The second type of metasurfaces is based on the geometrical phase, which appears when a light polarization is considered. Specifically, in case an anisotropic building block is illuminated by some polarized light, the block converts this polarization into any other polarization that is phase shifted by the block's rotation angle [24]. This geometrical phase, also called Pancharatnam-Berry phase [25], is often explained using a circular polarization. For example, left-circularly polarized light impinges on an anisotropic building block that acts as a half-wave plate. This half-wave plate generates right-circularly polarized light that is phase shifted. Considering such configuration, a complex transmitted electric field $\mathbf{E}_t$ can be explained as a superposition of the left- and right-circularly polarized light [26]

$$\mathbf{E}_t = \frac{t_l + t_s}{2} \begin{pmatrix} 1 \\ i \end{pmatrix} + \frac{t_l - t_s}{2} \exp(-i\phi_g) \begin{pmatrix} 1 \\ -i \end{pmatrix}, \tag{1.3}$$

where t_l and t_s are complex transmission coefficients for incident light, linearly polarized along the long (l) and short (s) anisotropic block axes, respectively, and

$$\phi_g = 2\theta \tag{1.4}$$

is the phase shift introduced to the generated polarized light by rotating the anisotropic building block by the rotation angle θ, relative to the reference coordinate system. It is important to mention that the Pancharatnam-Berry phase is purely geometric in nature and does not depend on frequency [26]. Therefore metasurfaces based on the geometric phase are broadband, but on the other hand limited to polarized light [27]. The following Table 1.1 sums up all the above-mentioned physical properties responsible for the phase shift in building blocks, and their advantages and limitations.

Table 1.1: Summary of physical properties responsible for the phase shift in metasurfaces.

	propagation-phase				Geometrical phase
	Plasmonic resonance	Gap-surface plasmon	Mie resonance	High aspect ratio	Pancharatnam-Berry
Materials	metal	metal–insulator–metal	dielectric	dielectric	metal, dielectric
Advantages	well-developed fabrication	high efficiency	Huygens metasurface	high efficiency	broadband
Limitations	low efficiency	reflective applications	limited by a coupling	complicated fabrication	polarized light

After describing metasurfaces on a microscopic level let us examine them from a macroscopic point of view. Based on its material, shape, lateral size or rotation, each building block induces a phase shift on a level of each nanopixel (spacing between two block centers). But what does the phase shift mean for light that illuminates the whole surface? Considering a planar wave perpendicularly impinging on an interface (as in Figure 1.2a), the Huygens-Fresnel principle might help to answer this question. The simplified version of this principle says that each point of a wavefront (in this case the interface) acts as a new point source of the wave, and the superposition of each new wave creates a new wavefront [1]. In case building blocks with a linear phase gradient are placed at the positions of these points, the planar wave might be bent to an angle that depends on this gradient and the nanopixel size (see Figure 1.2b).

It is important to note that this bent light is not the only light behind such metasurface. In reality, each point behind a transmissive or in front of a reflective metasurface represents a superposition of complex fields transmitted through or reflected from the surface and scattered by building blocks. However, in almost all metasurface applications only the superposition of scattered light is considered. Like in the case of light
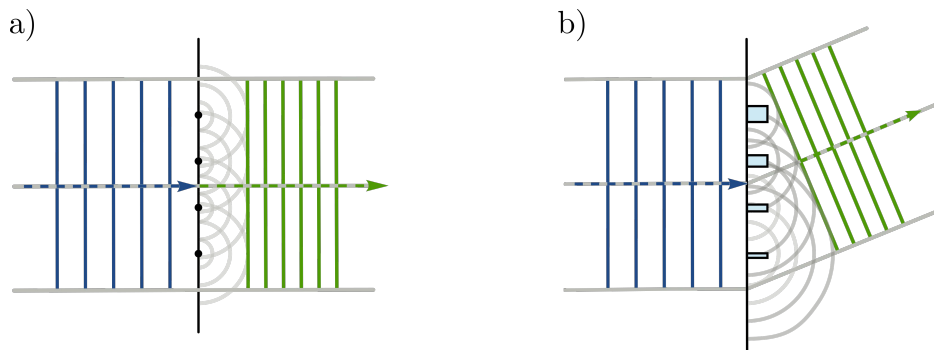

Figure 1.2: Huygens-Fresnel principle for metasurfaces. Scheme of a planar wave impinging perpendicularly on an unstructured interface a) and metasurface b). Adapted from [28].

bending, where the highlighted direction of transmitted light (Figure 1.2b) is just one specific direction in which scattered light interferes constructively.

In summary, any metasurface is composed of tiny structures called building blocks, which shift the phase of the electromagnetic wave by using propagation or geometric means. While the propagation-phase is based on the control of n_{eff} through various physical properties, the geometric phase, also called the Panchartnam-Berry phase, is based purely on geometrical configuration of the block, while considering cross-polarized light. When the phase gradient is properly chosen, building blocks can collectively act as a functional metasurface, with applications that are going to be described in the following section.

1.2   Applications

Having well-defined building blocks and choosing a metasurface function (e.g. metalens, beam-splitter, hologram), the next task is to find out how to position those building blocks to provide such function. The placement of blocks on a surface is determined by a phase map $\Phi(x,y)$. It represents the phase distribution on top of the surface to obtain the specific metasurface fucntion. The map can be achieved by one of two approaches: forward or inverse design.

The forward design is based on an analytically formulated phase map, which is calculated simply by inserting the known parameters into a theoretical formula. Nonetheless, analytical solutions are limited to only few most known metasurfaces, such as beam deflectors [29], metalenses [30], polarizers [31], axicons [32], and vortex beam generators [33].

The inverse design deals with more complicated metasurfaces such as metaholograms [34, 35], or beam splitters [36]. The phase map is calculated from a function describing the desired outcome using, for example, a generative model [37] or machine learning [38]. Even more complex way is to implement topological optimization that also works on inverse principle, but implements arbitrary scatterers rather than specific building blocks [39].

When obtaining the phase map for the desired metasurface function, the whole metasurface production process then might look as in Figure 1.3, where the metalens made of TiO_2 building blocks is designed, fabricated and measured. The process starts with establishing a building block library either by simulations or a phase measurement (as in case of Figure 1.3a). Then it continues with calculating the phase map following the forward (as in Figure 1.3b) or inverse design. Finally it ends up with filling and fabrica-

ting the metasurface with appropriate building blocks (Figure 1.3c) and subsequently measuring the functionality of the metasurface (Figure 1.3d).

Combining both design principles with a well-established building block library and precise fabrication already resulted in optical components with high efficiency [23, 40], working in the broadband spectrum [41, 42], without aberrations [43, 44], or with the possibility to actively tune already fabricated metasurface [45, 46]. As this thesis is about implementing a tunable phase-change material into a metasurface, the tunable metasurfaces will be now reviewed more closely.
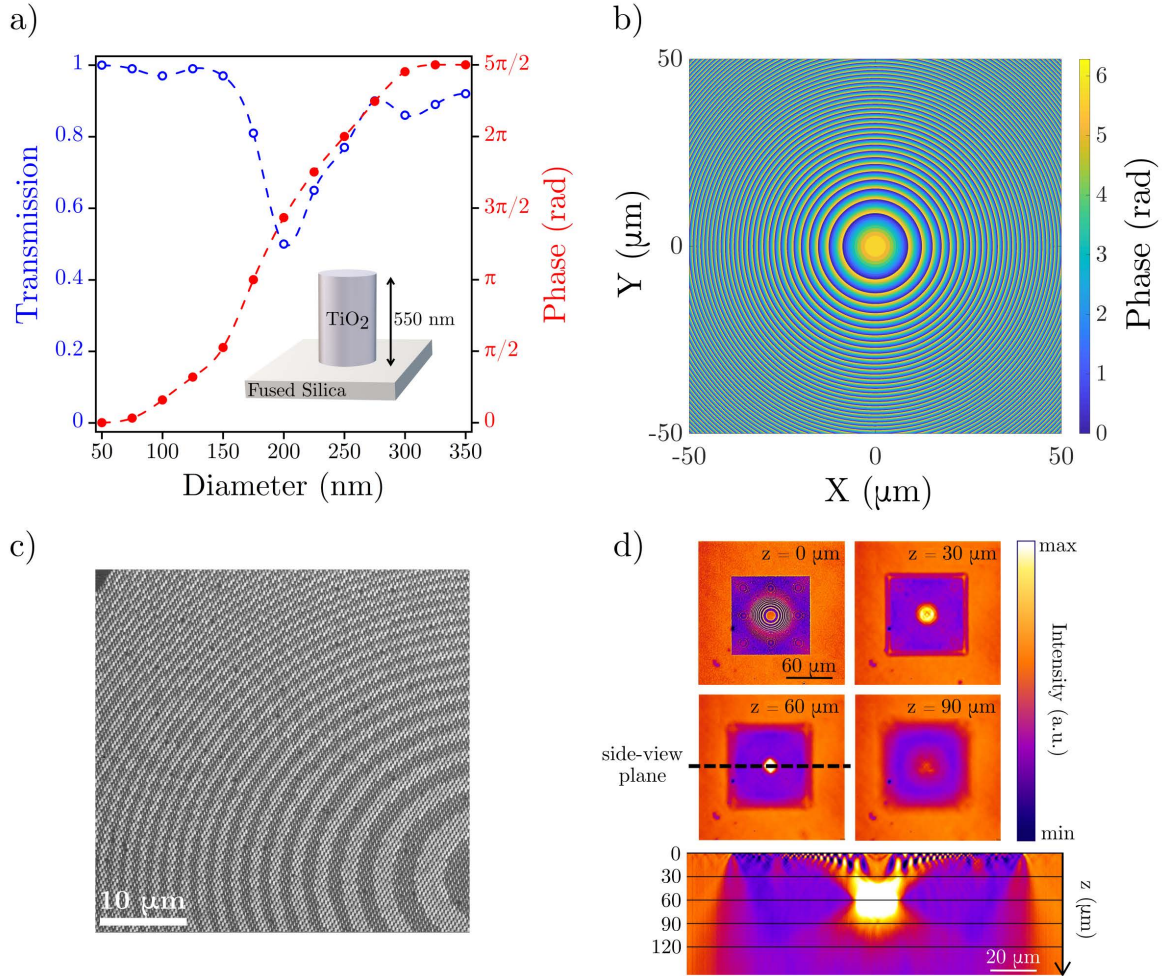
Figure 1.3: Metasurface production process. a) Building block library. transmission phase and amplitude measurement of TiO₂ building blocks as a function of their diameters. Adapted from [47]. b) Phase map. Analytical solution for a $100 \times 100\,\mu$m metalens with focal length $60\,\mu$m and operating wavelength $650\,$nm. Adapted from [47]. c) Fabrication. Scanning electron microscope (SEM) micrograph of a fabricated TiO₂ metalens. Adapted from [48]. d) Measurement. Light intensity z-scan of the metalens at $650\,$nm. Four top views at $0\,\mu$m, $30\,\mu$m, $60\,\mu$m, $90\,\mu$m behind the metasurface and one side-view in a plane highlighted by dashed line. Adapted from [48].

1.3 Tunable metasurfaces

Tunable metasurfaces are metasurfaces in which a shape or refractive index of building blocks can be altered after they were fabricated [49]. Altering the shape can be done by a flexible substrate [50] or by microelectromechanical systems (MEMS) [51]. Even though metasurfaces with flexible substrates or MEMS might be well controlled via specific strain (Figure 1.4a) or applied voltage (Figure 1.4b), size and complexity of such metasurfaces often limit their operational frequency or metasurface functionality in general.

Metasurfaces made of materials with tunable refractive index might overcome such limitations, as the size and complexity of metasurface building blocks can be reduced. The control over the refractive index can be achieved by a thermo-optic effect, a free-carrier effect, or a phase-transition [52].
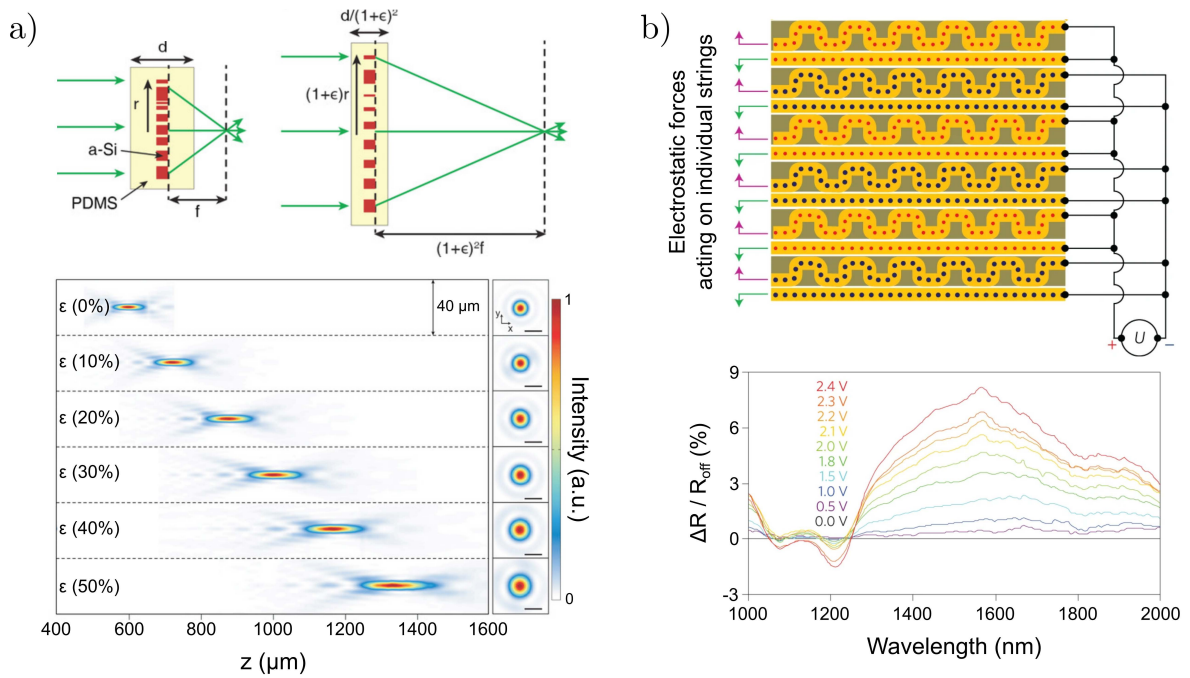
Figure 1.4: Tunable metasurfaces based on altering the shape. a) Tunable metalens made on top of the elastic substrate. Upper part represents side-view schemes of the tunable metalens made of silicon (a-Si) structures on a polydimethylsiloxane (PDMS) substrate. On the left the lens is relaxed, while on the right the lens is stretched by a stretch ratio $1 + \epsilon$. The graph in the lower part represents measured optical intensity profiles of a radially strained metasurface microlens in the axial plane (left) and the focal plane (right). Scale bars: $5\,\mu$m. [50]. b) Scheme of a MEMS plasmonic metasurface made of gold structures (top) and its reflection modulation measurement as a function of wavelength for different applied voltages listed in the graph (bottom) [53].

The thermo-optic effect refers to the phenomenon that refractive indices of materials change with temperature. Tunable metasurfaces made of silicon [54] (Figure 1.5a) or lead telluride [55], working in near-infrared and infrared region, respectively, were proposed using this principle. Huge drawbacks of such metasurfaces are high energy consumption and low modulation speed, which is limited by thermal transport properties.

The free-carrier effect is responsible for a change of refractive index due to modification of carrier densities and carrier effective masses. This principle has been utilized in metasurfaces made of semiconductors [56, 57] (Figure 1.5b), transparent conductive oxides [58, 59] (Figure 1.5c), and graphene [60, 61] (Figure 1.5d). Besides a regular tuning with still a high thermal energy consumption, the refractive index in most of these metasurfaces can be tuned even by an optical pump switching, which enables an ultra-fast modulation. However, a low energy difference between two excited states of free-carriers limits metasurfaces based on the free-carrier effect mostly to infrared (IR) or terahertz (THz) region [52].

Phase-transition represents a crystallographic change, where a shift of atom or molecule positions results in a change of the band structure and therefore of the refractive index. The most known and widely used phase-transition materials are liquid crystals (Figure 1.5e), which can be switched from nematic to isotropic configuration by thermal or electrical stimuli [62]. Liquid crystals are mostly used as an environment in which polarized incident light experiences a larger dielectric constant within the extraordinary axis of the nematic liquid crystal [63, 64]. Nonetheless, efficiency of such metasurfaces is limited due to micrometer pixel sizes, as liquid crystals can be hardly controlled on nanometer scale [65]. Another phase-transition material, known for its use in rewritable optical discs, is germanium–antimony–telluride (GST) [66]. It is a chalcogenide glass known for its transition from an amorphous to crystalline form [67]. As its crystallization temperature is around $150\,°C$, while the melting point back to its amorphous form is around $600\,°C$, GST represents a non-volatile material that keeps its refractive index after cooling back to room temperature [68]. Besides applications as a metasurface spacer [69, 70] or even a building block [71, 72], GST has been recently used in hybrid structures enabling NIR optical phase modulation (Figure 1.5f) within its two crystalline forms [73, 74]. Besides GST, there are also other promising chalcogenide glasses, such as stibnite (Sb_2S_3), that exhibit low-losses while altering high index modulation especially in the visible spectrum [75, 76], but due to their novelty in the context of nanophotonics they so far received less attention [77]. Another group of phase-transition materials are strongly correlated materials, such as cuprates, iron pnictides or dichalcogenides [78]. In these materials, electron correlations are so strong that they can not be ignored as for other materials and so strong that they result in

an altered band structure. Out of all strongly correlated materials, vanadium dioxide (VO_2) exhibits exceptional optical properties. As the main focus of this thesis, it will be discussed in more detail in the following chapter.

In summary, metasurfaces are nanostructured surfaces that control light through their building blocks, based on either propagation or geometric phase. While simple metasurfaces can be utilized following forward design, more complex metasurfaces require inverse approach. Using this inverse design and implementing both propagation and geometric phase together with tunable properties might increase functional possibilities or the efficiency of the whole metasurface. It is important to note that tunable metasurfaces based either on mechanical control or refractive index control suffer from a trade-off with operating frequencies, modulation depth, modulation speed, fabrication limitations, and high energy consumption. However, with or without these problems, tunable metasurfaces represent a next step in the development of metasurfaces.
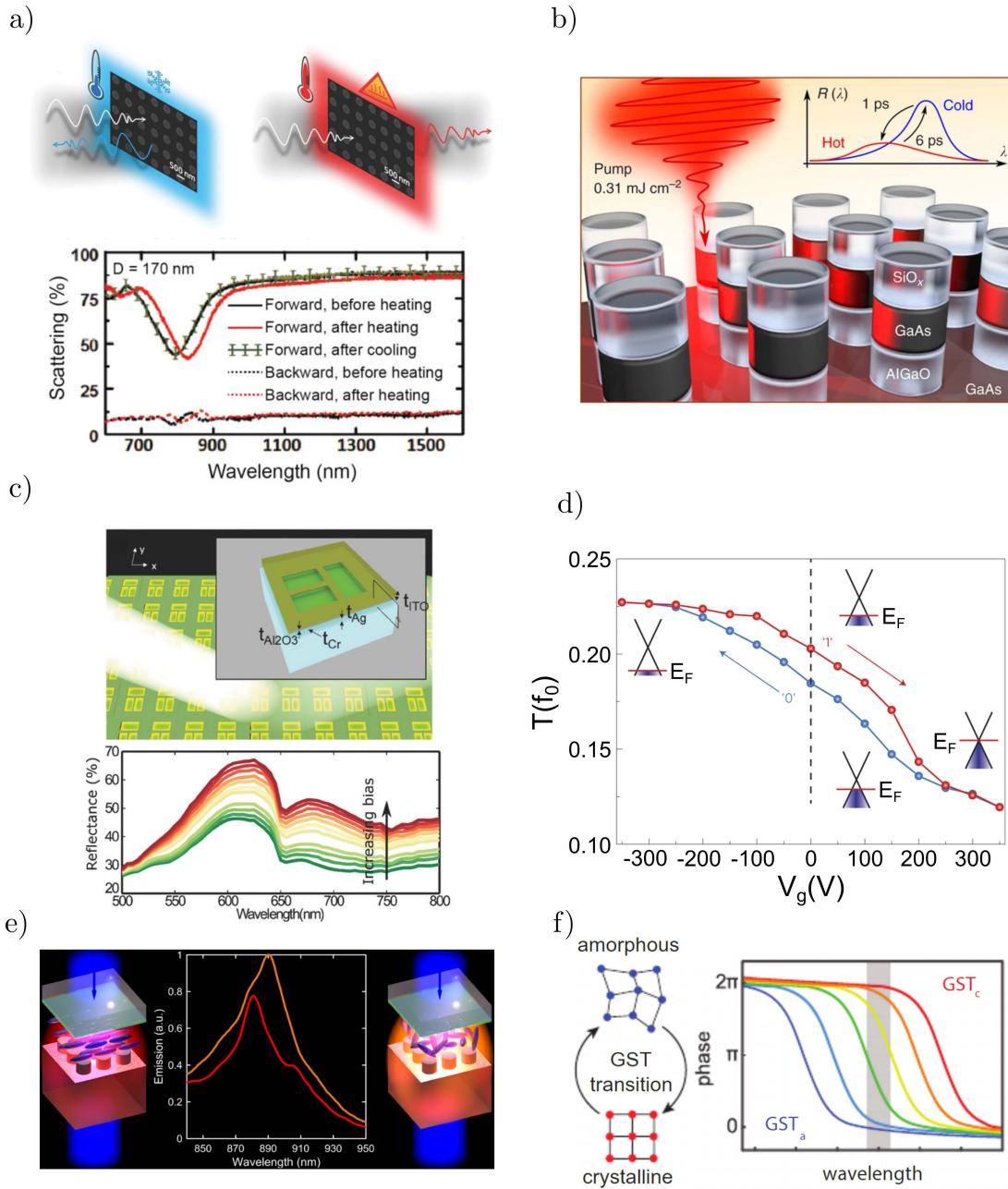
Figure 1.5: Tunable metasurfaces based on altering the refractive index. a) SEM micrograph of a tunable Si metasurface based on a thermo-optic effect (top) and measured forward and backward scattering as a function of wavelength at $20\,°C$ and $300\,°C$ (bottom) [54]. b) Scheme of a GaAs dielectric optical metasurface with inset of illustrative reflectance change during an ultrafast switching by optical pumping [57]. c) Scheme (top) and reflectance measurement (bottom) of a metasurface with indium tin oxide on top of dolmen structures, tunable via increasing voltage between top and bottom films [58]. d) Transmission hysteresis of a graphene-based metasurface as a function of bias voltage [60]. e) Scheme of a metasurface using liquid crystals and a light emission measurement as a function of wavelength during thermal actuation [62]. f) All-dielectric programmable Huygens' metasurface, incorporating GST in a sandwich-like structure that enables optical phase modulation within its two crystalline forms [74].

2.   Vanadium dioxide

Whereas phase-change materials (PCMs) represent a huge group of materials that a crystal structure can be changed by applied energy, there are only a few that are well-suited for tunable metasurface applications. Well-suited PCMs are the ones with ideally a solid to solid transition and a considerable refractive index modulation during the transition. Previously mentioned chalcogenide glasses represent such well-suited PCMs, which are attractive due to their non-volatile memory transition. Vanadium dioxide (VO_2) stands out as another unique PCM for its volatile transition with an ultra-fast switching properties [79] and a significant optical modulation in NIR region [80].

The following part of this thesis moves on to describe in greater detail the physics and origin of the VO_2 phase-transition, and deposition techniques used for fabricating this material. The next part of this chapter will be focused on the influence of various deposition techniques and of the quality of VO_2 on the magnitude of its refractive index modulation. Lastly, the current state of the art applications of VO_2 in metasurfaces will be discussed.

2.1   Physics of vanadium dioxide

VO_2 uniqueness lies in its insulator to metal transition (IMT) occurring already around 67 °C and associated with a major change in its resistivity [81] and optical properties [80]. A change in resistivity of four orders of magnitude during VO_2 IMT was discovered by F. J. Morin already in 1959 [82]. Since then, the physics behind this transition is still under debate [83].

On one hand, VO_2 is proved to behave as a Mott insulator, in which a regular band theory falls apart because of strong electron–electron Coulombic repulsion [84]. Such repulsion freezes electrons in space and prevents electrical conduction. Temperatures above 67 °C brake such state, making electrons free carriers again. This is what makes VO_2 a strongly correlated material and questions the categorization of VO_2 as a phase-change material.

On the other hand, VO_2 also exhibits a structural change during the IMT [83]. In the case VO_2 is fabricated without doping or high pressure, it changes from a monoclinic phase M1 with $P2_1/c$ space group at room temperature to a rutile phase R with a tetragonal unit cell and $P4_2/mnm$ space group at temperatures above 67 °C. Using specific doping or strain, other phases such as a monoclinic M2 with $C2/m$ space group, or a triclinic T with P1 space group can be obtained [85]. However, such metamorphs are unstable during the transition [85] and therefore VO_2 undergoes mostly the monoclinic to rutile transition. This transition causes lattice distortion, described by Peierls strong dimerization [86], which is responsible for a change in ion positions and the subsequent change in the band structure (Figure 2.1). More detailed description and explanation of both transition processes can be find in the works of Eyert [87] or Wentzcovitch *et al.* [88].

The combination of both transition processes is what makes VO_2 a very promising PCM, as an external stimuli responsible for the transition does not need to have only a thermal character. The VO_2 transition can be triggered also by optical heating using a continuous wave (CW) laser [89], electric field (E-field) [90], THz field [91] or by a nonlinear effect using a femtosecond (fs) laser [92]. While switching speeds of thermal and electrical external stimuli are limited by their physical character, the possible use of the fs laser proves VO_2 ultrafast switching capabilities. For better visualization of the respective time-scales, all the above-mentioned external stimuli of the VO_2 transition are illustrated with their experimentally verified switching speed-ranges in Figure 2.2.

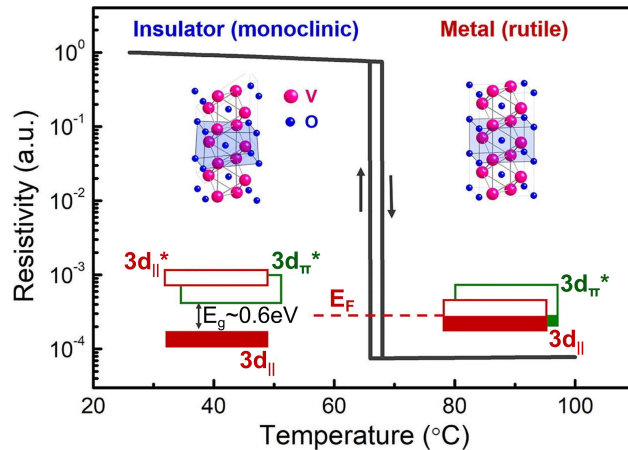**Figure 2.1:** An illustrative resistivity hysteresis of VO_2 as a function of temperature. Upper insets show a simulated monoclinic and rutile structures of VO_2. Lower insets show an illustrative change of the VO_2 band structure, where split $3d_{\parallel}$ band on the left creates the band gap E_g and the band structure on the right shows a metallic character of VO_2. Adapted from [93].
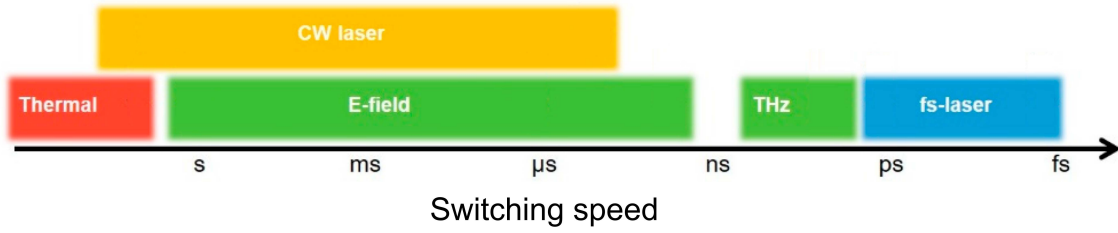
Figure 2.2: Scheme of experimentally verified switching speed-ranges of various external stimuli for the VO$_2$ phase-transition. Adapted from [94].

To employ possibilities of all these external stimuli and to utilize VO$_2$ structural, electrical, and optical potential, a high-quality VO$_2$ has to be fabricated first. Besides a vapor transport or a hydrothermal method which are mostly used for fabrication of VO$_2$ nanowires, techniques like magnetron sputtering, pulsed laser deposition (PLD), chemical vapor deposition (CVD), evaporation or sol-gel synthesis are used for fabrication of VO$_2$ thin films [85]. Nonetheless, the fabrication process is not straightforward. The quality of VO$_2$ is affected by many factors such as a multivalence state of V element (Figure 2.3), crystallinity [95] and strain introduced by the thin film thickness [96] or the substrate [97]. These factors can be controlled by deposition parameters, specific for each technique. Hence, for any kind of VO$_2$ application a careful optimization of the chosen deposition technique has to be carried out beforehand.
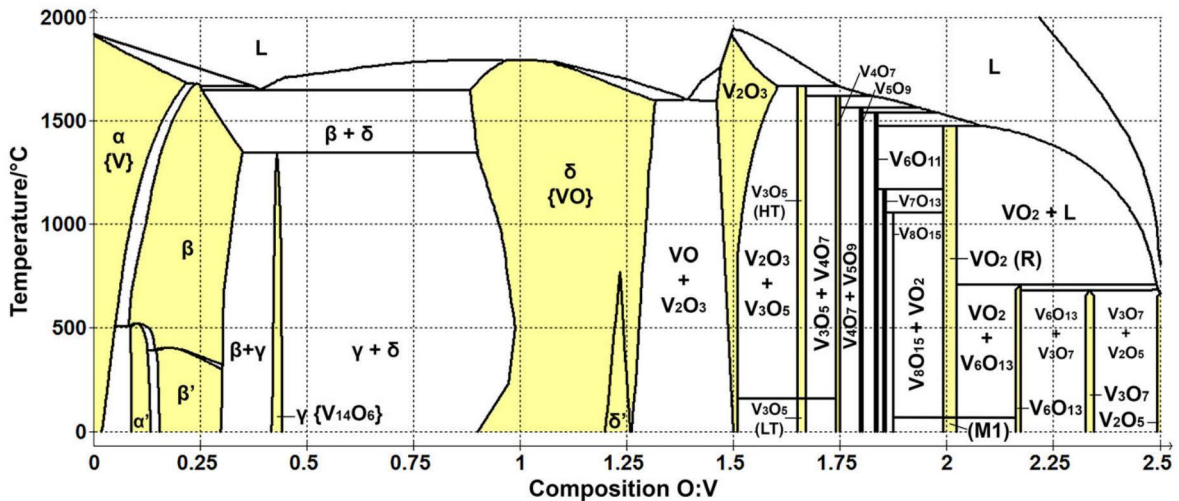
Figure 2.3: A vanadium–oxygen phase diagram. From left to right, vanadium as a metal in α, β, γ and δ solid phases change into vanadium oxide phases with the increasing oxygen content. When heated above the specific temperature, solid phases change into the liquid phase (L). Highlighted parts represent the single-phase regions. Adapted from [98].

But what is a good figure of merit to compare VO_2 after the deposition? There are several techniques that might provide a different type of information about the VO_2 quality. For example, X-ray photoelectron spectroscopy (XPS) is used for stoichiometry analysis, X-ray diffraction (XRD) for crystallinity investigation, atomic force microscopy (AFM) for morphology, and Raman spectroscopy for defects and dynamic structural transformation analysis. However, all these appointed techniques give the specific structural information. To obtain more general information about VO_2 electrical or optical properties, other techniques such as resistivity measurements, optical pump-probe, or optical spectroscopic measurements have to be employed. Whereas the combination of all these information is crucial for full understanding of the VO_2 transition and its quality, some information might be redundant for specific VO_2 applications. This is the case for VO_2 in nanophotonic applications like metasurfaces, where overall knowledge about the transition might be useful, but what really matters is the optical absorption and the refractive index modulation during the IMT. The following section will be therefore focused on the refractive index difference during the transition and various influences that affect optical properties of VO_2.

2.2   Refractive index

Vanadium dioxide undergoes a phase-transition from an insulator (dielectric) form to a metallic form, during which an abrupt change in its band structure occurs. The change in the band structure is bound to the change of its complex refractive index. Just to remind that the complex refractive index consists of its real part (n), often referred to as the refractive index, and its imaginary part (k), also called the absorption coefficient. Besides its abrupt shift in the refractive index and zero absorption in the dielectric form in THz region [94], VO_2 is mostly sought after for its significant index transition and low absorption in the VIS and NIR region (Figure 2.4a, b). The absorption and refractive index difference during the transition thus represent good figures of merit based on which VO_2 quality can be evaluated.

In Figure 2.4 we can see a library of more than 80 refractive indices and absorption coefficients of VO_2 in its dielectric (light blue lines) and metallic (light red lines) form. This library was created mostly by extracting complex refractive indices or dielectric functions from scientific articles (as referenced in Figure 2.4) and it was created due to three reasons:

The first reason was to observe general spectral trends of the complex refractive index of VO_2 and its behaviour during the phase-transition. It came out that due to
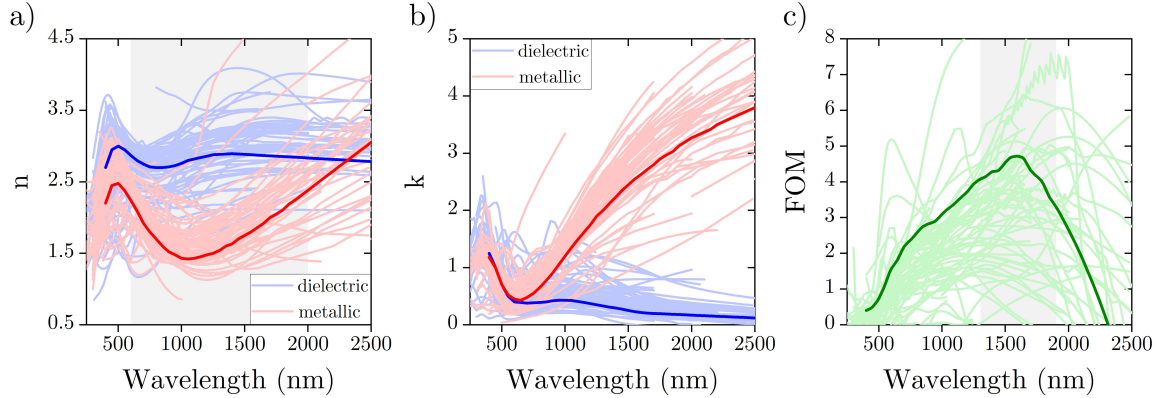
Figure 2.4: Large dataset of VO_2 a) refractive indices and b) absorption coefficients spectra in the dielectric (blue) and metallic (red) form. Extracted from [80, 81, 99–176]. c) Figure of merit (FOM) calculated from a) and b). Thick lines in all graphs represent VO_2 with relatively high FOM across both VIS and NIR region (Ref. [177]).

the transition, VO_2 exhibits refractive index difference of approximately $0.5 - 1.5$ in the wavelength region between $600 - 2000$ nm. In Figure 2.4b we can see that up to 600 nm wavelength, the VO_2 is a lossy material that has almost the same absorption coefficient in both its forms. However, above 600 nm, VO_2 absorption in the dielectric form significantly decreases, while in the metallic form, VO_2 becomes a strongly absorbing material.

The second reason for creating the library was to have a reference for quality assessment of VO_2 fabricated by our group. Unfortunately, it was too hard to simultaneously compare our VO_2 refractive index difference during its transition together with the magnitude of the absorption coefficient with so many competitors from the library.

The third reason for creating the library was to set a limit for our expectations regarding the best possible performance that VO_2 can do in the field of metasurfaces, or generally in nanophotonics. But again, it was hard to simultaneously set the expectation limit for both the refractive index difference and the absorption.

Due to this difficulty, we established our own figure of merit (FOM) that includes both of these factors and is defined as

$$\text{FOM} = \frac{n_{\text{dielectric}} - n_{\text{metallic}}}{k_{\text{dielectric}}}. \tag{2.1}$$

Note that a similar FOM was defined by Gutiérrez *et al.* [76], who used Δk instead of $k_{\text{dielectric}}$. We find $k_{\text{dielectric}}$ to be more relevant as most applications are focused on a low-absorbing dielectric form of VO_2 and the information about the metallic form absorption is interesting only in the context of switchable absorbers [111, 178].

The FOM proves to be a perfect tool for quality assessment of VO_2 and a perfect tool to find out the best fabricated VO_2. In Figure 2.4c we can see FOMs calculated from refractive indices and absorptions in Figure 2.4a and b, respectively. A general trend of the plotted lines clearly shows that the VO_2 transition is the best (i.e., offers big refractive index difference with only low absorption) between $1400 - 2000\,nm$ wavelengths. This confirms and visualizes the eminent position VO_2 has at telecommunication wavelengths [179]. The highlighted lines in all three graphs of Figure 2.4 represent one specific VO_2 film which serves as an example. It was chosen because its refractive index in the dielectric form is not too high when compared to others and the absorption is not the lowest compared to other VO_2 films, but it still exhibits very high FOM. This means that even though it does not seem to be the best in any of separate optical factors compare to other films, the combination of these factors makes such film a very promising for metasurfaces in the VIS and NIR region.

In many articles, the optical response of VO_2 is often connected to its crystallinity. Specifically, a better VO_2 crystal structure (less defects, bigger grains or a lower substrate lattice mismatch) results in more pronounced static resistivity modulation during the transition, and this *resistivity* modulation is often considered as a proxy also to big *optical* modulation [83, 116]. While the first statement about the relationship between resistivity modulation and crystallinity is supported quantitatively by many articles [106, 107, 180], the second statement about high resistivity modulation being equivalent to high optical modulation is not properly supported by evidence, especially in the VIS and NIR region. Having our library of refractive indices with the appropriate FOM creates a great tool for investigation of such statement.

As deposition techniques and their parameters used for VO_2 fabrication tend to have a huge impact on VO_2 stoichiometry and crystallinity [117], we decided to compare FOMs of VO_2 prepared by different techniques first. In Figure 2.5a we can see that VO_2 thin films of various quality can be fabricated by magnetron sputtering, which is also the most often used technique to deposit VO_2. The huge spread in FOM may suggest that magnetron sputtering parameters need to be carefully adapted. Contrary, PLD, with its usually better-controlled environment, can provide films with higher FOM (Figure 2.5b), making it probably less sensitive to the specific deposition parameters. No matter how tempting, such certain conclusion can not be made as the number of data, compare to magnetron sputtering, is significantly lower. Other techniques, such as electron beam evaporation, sol-gel synthesis, ALD or MBE seem to be able to provide also VO_2 with high FOM (Figure 2.5c), but the number of samples in the graph is statistically insufficient to support such conclusion. It is obvious that deposition techniques and their parameters have large impact on VO_2 properties . But
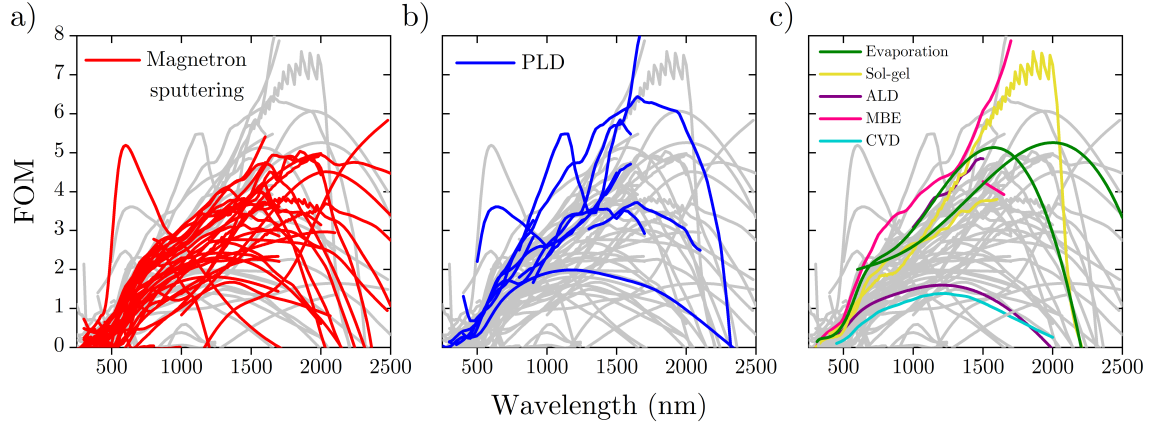
Figure 2.5: FOM spectra of VO$_2$ films deposited by a) magnetron sputtering, b) PLD, c) electron beam evaporation, sol-gel synthesis, ALD, MBE, and CVD. Grey lines represent FOMs of VO$_2$ deposited by other methods than those listed in the specific graph. Calculated from [80, 81, 99–177].

to find a proper connection between the FOM and crystallinity, we must look closer on the influence of a substrate or of a film thickness.

The substrate underneath has a significant impact on the VO$_2$ crystallinity and therefore optical properties. This impact arises from the mismatch of the substrate and VO$_2$ lattice constants, and it influences VO$_2$ especially at the beginning of the deposition. That means, if there is large lattice mismatch, or the substrate tends to have amorphous character, VO$_2$ is grown in a polycrystalline manner. This polycrystalline VO$_2$ and its optical modulation is furthermore controlled by its crystal grains and defects, of which quantities and sizes depend on the film thickness and deposition parameters [96, 181, 182]. This is the case of VO$_2$ deposited on substrates such as silicon, quartz or other glasses on which VO$_2$ grows in polycrystalline form. Because of varying thicknesses and grain sizes in the available literature the extracted FOM also exhibits significant variability for all these substrates (Figure 2.6a, b, c).

Contrary, when lattice constants of the substrate are close to those of VO$_2$, the thin film tends to grow epitaxially as a single crystal. This epitaxial film is however limited only to the certain thickness. Because lattice constants are not matching, VO$_2$ experiences strain, which depending on the substrate orientation or deposition parameters can sustain up to approximately 20 nm [183]. In thicker films, this strain relaxes through various defects, which disrupt the VO$_2$ crystallinity. Despite this imperfect lattice matching, VO$_2$ on top of substrates such as c-plane sapphire or TiO$_2$ has better crystallinity than VO$_2$ grown on amorphous or more significantly mismatched substrates, and it exhibits higher resistivity contrast during the VO$_2$ transition [81, 99]. The high resistivity contrast, often wrongly extrapolated to a high optical contrast, does not
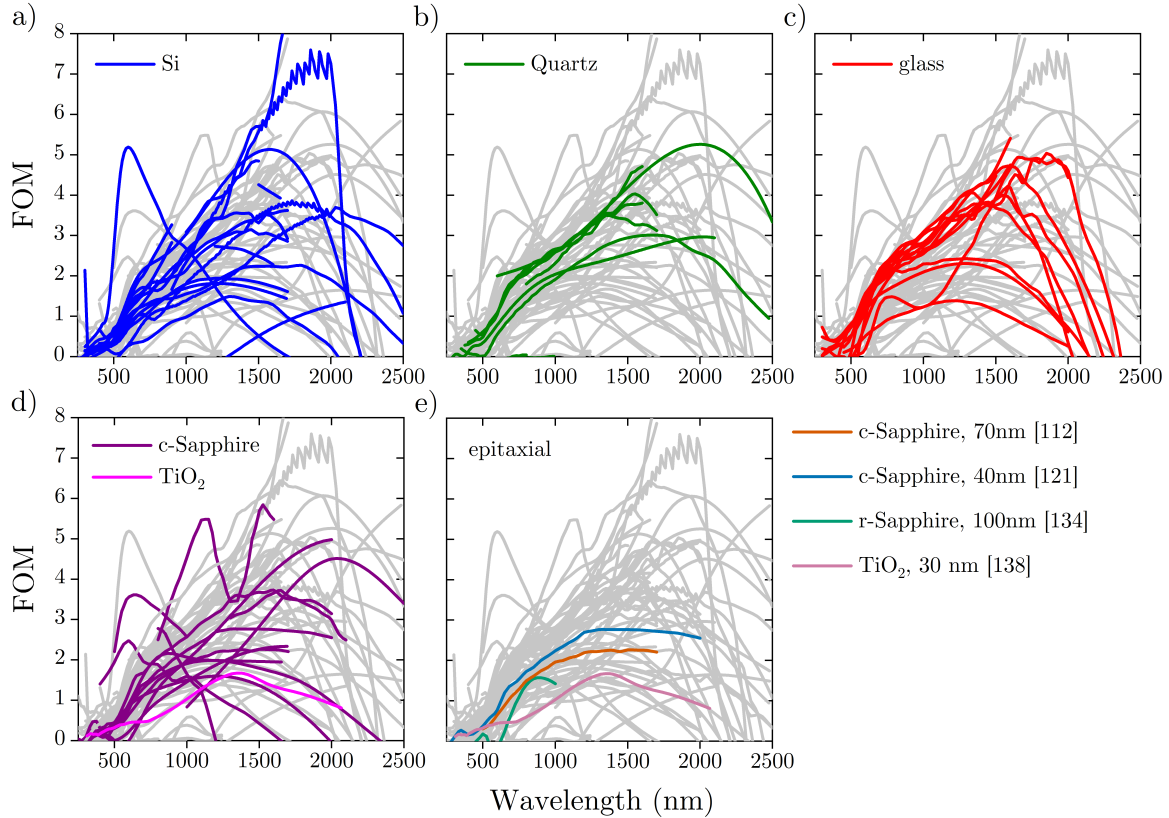
Figure 2.6: FOM spectra of VO$_2$ films deposited on a) silicon, b) quartz, c) glass, d) c-plane sapphire and TiO$_2$. e) FOMs of epitaxial VO$_2$ films grown on various substrates listed in the graph together with relevant thicknesses. Grey lines represent FOMs of VO$_2$ deposited on other substrates than those listed in the specific graph. Calculated from [80, 81, 99–177].

result in the high FOM in the VIS and NIR region (as shown in Figure 2.6d). We can see that VO$_2$ with supposedly better crystallinity on c-plane sapphire or TiO$_2$ substrates exhibits similar or in some cases even worse FOM compared to its highly polycrystalline counterpart (Figure 2.6a). These findings suggest that better crystallinity and higher resistivity modulation do not necessarily result in high optical modulation in the VIS and NIR spectral region. This notion is supported also by very low FOM for thin films reported as epitaxial films grown by magnetron sputtering on sapphire or TiO$_2$ substrates, exhibiting four orders of magnitude resistivity modulation (Figure 2.6e).

These findings rise many new questions, such as what influences VO$_2$ optical modulation in the VIS and NIR region and how the high static resistivity modulation during the transition is or is not connected to the optical properties. Answering such questions would require deeper examination that is far beyond the scope of this thesis. The information that a perfectly crystalline VO$_2$ does not necessarily result in a significant optical modulation in the VIS and NIR region has at least two consequences.

The first consequence is that low-loss VO_2 with high refractive index contrast in the VIS and NIR region can be fabricated on any substrate using any deposition technique. The second consequence, in case a nanophotonic application is concerned, is to evaluate VO_2 quality using transmission spectroscopy or spectroscopic ellipsometry rather than using a resistivity measurement, XRD or other techniques. Utilizing these new findings could make VO_2 more attractive, as we think that wrong quality factors and complicated fabrication resulted in less metasurface applications of VO_2 in the NIR and VIS region. Applications, which we would like to devote the following section.

2.3   State of the art in metasurfaces

Due to its structural, electrical and optical modulation during the phase-transition, VO_2 has been applied in various fields of interest. While there are works utilizing VO_2 for electromechanical tunning [184], thermochromic window coatings [185], waveguides [83], or even for electromagnetic wave manipulation in the THz region [94], there are far less works facilitating VO_2 for light manipulation in the VIS and NIR region.

The most work in the VIS and NIR area has been done on unstructured thin films of VO_2, which has been used directly as a tunable absorber [111, 179], or indirectly as a substrate under metal structures [186–189], where it enabled tuning of their plasmonic resonances (Figure 2.7). In case of structured VO_2, there are articles where pure [100, 105, 118], or hybrid [101, 103] nanostructures are applied for a control of reflected, or transmitted light (Figure 2.8). While most of these applications in the VIS and NIR region can be already considered as tunable metasurfaces there are only few works where full investigation of amplitude, phase and polarization is examined [114, 190–195]. As most of these works use gap surface plasmon metasurfaces (Figure 2.9), transmissive tunable metasurfaces in the VIS and NIR region stay highly untouched.

In summary, the beginning of this chapter was devoted to the physics of the VO_2 phase-transition. We showed that the structural change and strong electron correlation cause large electrical and optical modulation during the VO_2 IMT already at low energies. This energy can be provided by all sorts of external stimuli, where each has its specific switching speed. The closer look was given to the optical modulation, where we showed that good crystallinity is surprisingly not connected to low-loss VO_2 with a big refractive index difference during the transition in the VIS and NIR region. Lastly, we also suggested that due to wrongly chosen quality factor, VO_2 applications for tunable metasurfaces in the VIS and NIR region stay highly untouched.
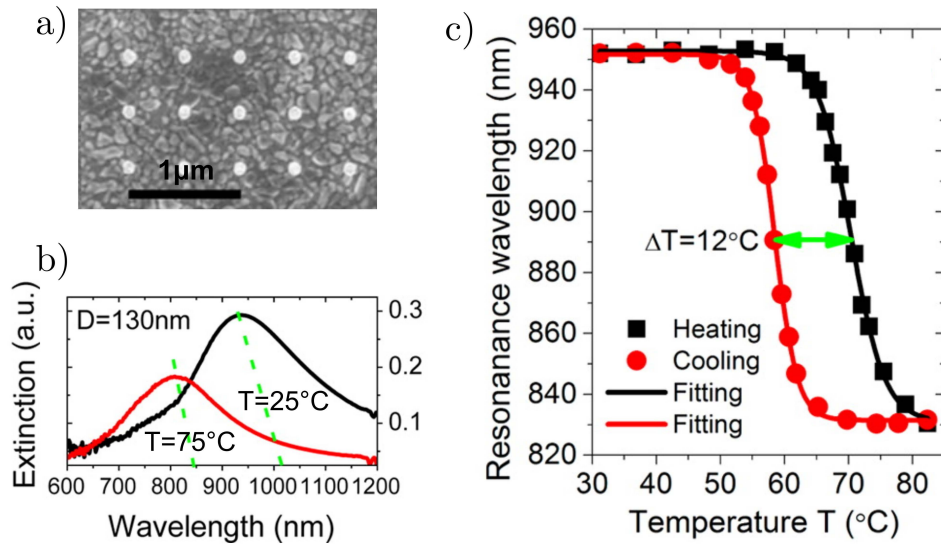
Figure 2.7: Plasmonic resonances of metal nanostructures fabricated on top of a VO$_2$ thin film. a) SEM micrograph of 130 nm gold nanocylinders on a 50 nm thick VO$_2$ film. b) Extinction of these nanocylinders as a function of wavelength, measured at 25 °C and 75 °C. c) Resonance wavelength hysteresis of b) as a function of temperature during the heating and cooling cycle. Adapted from [188].
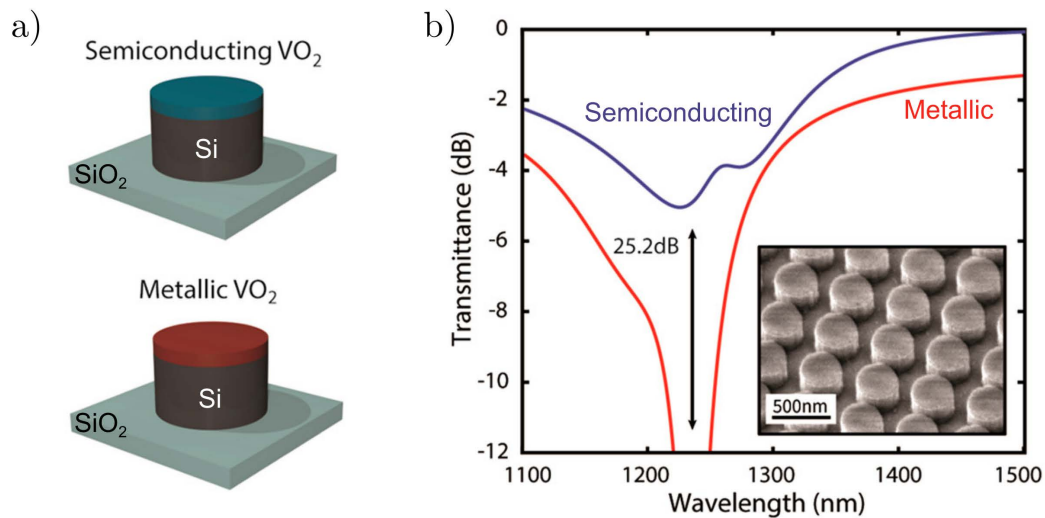
Figure 2.8: a) Scheme of hybrid silicon–VO$_2$ nanocylinder in a semiconducting and metallic state of VO$_2$. b) Simulated transmittance of the hybrid nanocylinder array with 475 nm diameters, 660 nm spacing, 190 nm silicon and 35 nm VO$_2$ thickness. The inset shows a SEM micrograph of those simulated structures. Adapted from [103].
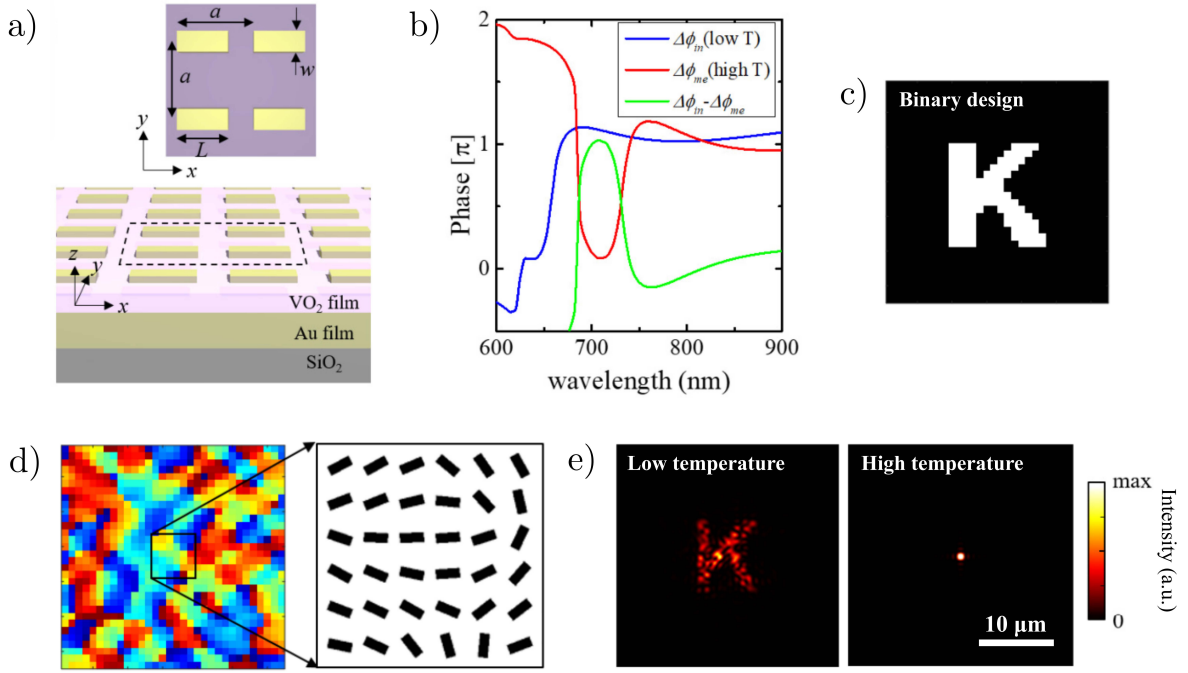
Figure 2.9: Tunable gap surface plasmon metasurface based on the Pancharatnam-Berry phase, incorporating a 30 nm-thick VO$_2$ film. a) Scheme of building blocks with length (L), width (w) and period (a). b) Phase-difference spectra $\Delta\phi$ between long (l) and short (s) axis polarizations at low (blue) and high (red) temperature, and phase spectrum subtracting the two spectra (green) for L=200 nm, w=80 nm and a=300 nm. c) Binary design of a Fourier hologram generated by the VO$_2$ gap surface plasmon metasurface. d) Phase map of the Fourier hologram c) with a magnified view of Au nanorod building blocks. e) Reconstructed far-field images at 700 nm wavelength at low and high temperature. Adapted from [193].

3.   Methods

To fabricate and characterize vanadium dioxide thin films and structures, various methods have to be applied. In the following chapter, we will introduce methods used within this thesis and provide a short description on how their results are processed.

3.1   Electron beam evaporation

An electron beam (e-beam) evaporation is a vacuum evaporation process, which falls into a group of physical vapor deposition (PVD) techniques. Its advantages, compared to other PVD techniques such as magnetron sputtering or pulsed laser deposition (PLD), are high deposition rate, better control over the thickness of the deposited material and higher number of substrates that can be inserted into the vacuum chamber [196]. E-beam evaporation is a process during which a material, called evaporant, is placed into a crucible and heated by a focused e-beam (Figure 3.1). The evaporated material is deposited on top of a sample that is placed above the crucible. Due to this configuration, a source of electrons is mostly placed beneath the crucible and the e-beam is bent into the crucible by a magnetic field (Figure 3.1). The deposition rate, which is controlled by beam voltage and current, can reach values up to few Ångstroms per second. Such high rates and the simplicity of the process are the reasons why e-beam evaporation is often used for deposition of metals or some simple oxides. However, high rates can also result in less control over quality of the material. For this reason, a sample heater and a gas injection system can be added to the evaporator, while making it more complex though. Moreover, oxygen injection can be added only in case that the electron source is not a tungsten filament, which would burn out in such atmosphere. The last thing to remember is vapor directionality, which is responsible for a different thickness of the deposited material over the sample [197]. To sustain as equal thickness over the whole sample as possible, the rotation of the sample holder can be used (Figure 3.1).
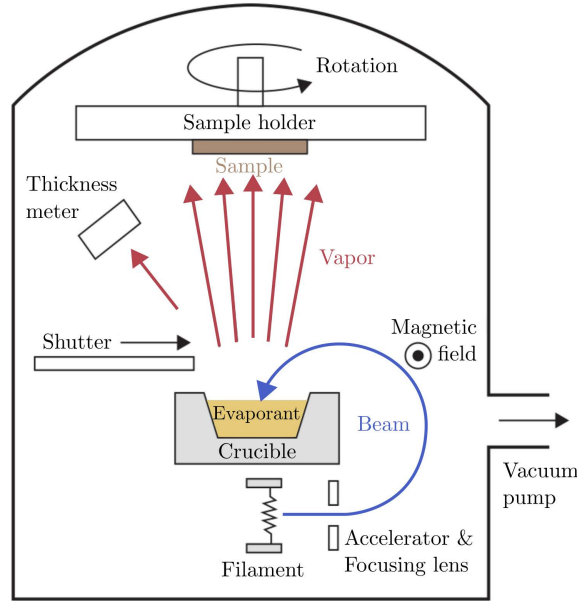
Figure 3.1: Scheme of an evaporator. The e-beam (blue arrow) is accelerated and bent by magnetic field into a crucible filled with evaporant. The evaporated material (red arrows) is then deposited on top of the sample. Adapted from [198].

3.2 Spectroscopic ellipsometry

There are many spectroscopic techniques that, by measuring certain macroscopic information, can describe a material at the atomic scale. Spectroscopic ellipsometry is one such technique. It is a powerful but complex tool for obtaining the dielectric function or precise thickness from an optical response of a thin film. In the following, a simplified explanation of two inseparable parts of spectroscopic ellipsometry, a measurement and analysis of the sample's optical response, will be provided.
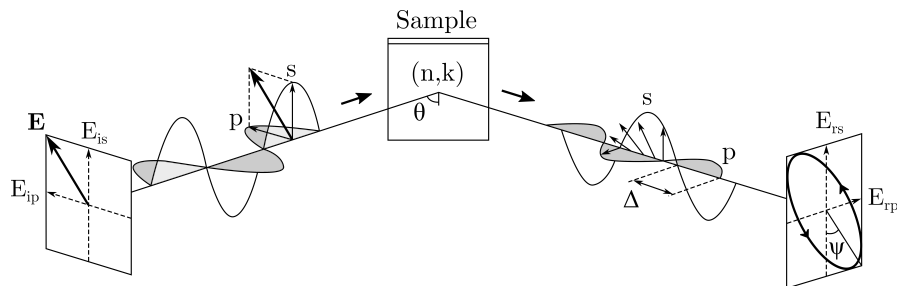
Figure 3.2: Spectroscopic ellipsometry: principle of a measurement. Linearly polarized electromagnetic wave impinges on a sample under the specific angle θ. The reflected wave with altered polarization is collected by a detector. From the detected intensity, which is a function of an analyzing component's angle, the ratio and the phase difference between p- and s- polarizations are calculated. Adapted from [199].

The spectroscopic ellipsometry measurement is based on a change of a polarized electromagnetic wave upon its reflection on or transmission through a sample (mostly reflection). Specifically, amplitude ratio ψ and phase difference Δ between p- and s-polarizations reflected from the sample are measured (Figure 3.2). The (ψ, Δ) pairs are defined from the ratio of complex amplitude reflection coefficients for p- and s-polarizations as [199]

$$\rho \equiv \tan \psi \exp(\mathrm{i}\Delta) \equiv \frac{r_{\mathrm{p}}}{r_{\mathrm{s}}}. \tag{3.1}$$

These two coefficients describe the probed sample, which by using Jones matrix formalism [22] can be defined as

$$\mathbf{S} = \begin{bmatrix} r_{\mathrm{p}} & 0 \\ 0 & r_{\mathrm{s}} \end{bmatrix} = r_{\mathrm{s}} \begin{bmatrix} \tan \psi \exp(\mathrm{i}\Delta) & 0 \\ 0 & 1 \end{bmatrix} = \frac{r_{\mathrm{s}}}{\cos \psi} \begin{bmatrix} \sin \psi \exp(\mathrm{i}\Delta) & 0 \\ 0 & \cos \psi \end{bmatrix}, \tag{3.2}$$

where the proportionality constant $\frac{r_{\mathrm{s}}}{\cos \psi}$ can be neglected since spectroscopic ellipsometry accounts only for relative changes in terms of intensity. The coefficients of this sample matrix can be determined by one of four ellipsometry configurations [199]. In the following, the explanatory calculation of the sample matrix will be provided, using the simplest configuration of rotating-analyzer ellipsometry (PSA$_{\mathrm{R}}$).

In the PSA$_{\mathrm{R}}$ configuration, the ellipsometer is composed of light source (L), polarizer (P), sample (S), rotating analyzer (A$_{\mathrm{R}}$) and detector (D). The configuration can be expressed using the Jones formalism as

$$\mathbf{L}_{\mathrm{out}} = \mathbf{A}\mathbf{R}(A)\,\mathbf{S}\mathbf{R}(-P)\,\mathbf{P}\mathbf{L}_{\mathrm{in}}, \tag{3.3}$$

where $\mathbf{L}_{\mathrm{out}}$ is Jones vector of the detected light, $\mathbf{A}$ is the analyzer Jones matrix, A is the analyzer rotation angle, $\mathbf{R}(A)$ is the analyzer rotation matrix, $\mathbf{S}$ is the sample matrix, $\mathbf{P}$ is the polarizer matrix, P is the polarizer rotation angle, $\mathbf{R}(-P)$ is the polarizer rotation matrix and $\mathbf{L}_{\mathrm{out}}$ represents normalized Jones vector of the incident light. Using the Jones matrix representation of these components, the Equation 3.3 can be rewritten into

$$\begin{aligned} \begin{bmatrix} E_{\mathrm{A}} \\ 0 \end{bmatrix} &= \begin{bmatrix} 1 & 0 \\ 0 & 0 \end{bmatrix} \begin{bmatrix} \cos A & \sin A \\ -\sin A & \cos A \end{bmatrix} \begin{bmatrix} \sin \psi \exp(\mathrm{i}\Delta) & 0 \\ 0 & \cos \psi \end{bmatrix} \\ &\quad \times \begin{bmatrix} \cos P & -\sin P \\ \sin P & \cos P \end{bmatrix} \begin{bmatrix} 1 & 0 \\ 0 & 0 \end{bmatrix} \begin{bmatrix} 1 \\ 0 \end{bmatrix}, \end{aligned} \tag{3.4}$$

where E_A is electric field of the reflected light as a function of the analyzer angle A. Expanding and recalculating this equation provides a relation between the measured intensity, the analyzer rotation angle and the (ψ, Δ) coefficients as

$$
\begin{aligned}
I &= |E_A|^2 \\
&= I_0 \left(1 - \cos 2\psi \cos 2A + \sin 2\psi \cos \Delta \sin 2A\right) \\
&= I_0 \left(1 + \alpha \cos 2\omega t + \beta \sin 2\omega t\right),
\end{aligned}
\tag{3.5}
$$

where the analyzer is motorized and the angle A can be replaced by a time-varying factor ωt, and $\alpha = \cos 2\psi$ and $\beta = \sin 2\psi \cos \Delta$ represent Fourier coefficients of $\cos 2A$ and $\sin 2A$, respectively. That means the (ψ, Δ) are obtained for each desired wavelength from fast Fourier transformation of the measured intensity. Despite the simplicity of the PSA_R configuration, this method fails to distinguish left-circular polarization from right-circular polarization since both these polarizations result in the same light intensity variation versus the analyzer angle [199]. To overcome such problem a fixed compensator, a rotating compensator or a phase modulator must be added, making the whole configuration and calculation more robust.

The (ψ, Δ) coefficients describe the optical response of the whole sample, which means the overall response of all layers that form the sample. In order to obtain the dielectric function or the thickness of one specific layer, it is necessary to perform ellipsometry data analysis that consists mostly of a construction of an optical model, dielectric function modeling, and fitting to the measured (ψ, Δ) spectra (Figure 3.3).

The optical model depends on the real sample arrangement. It can be constructed by one bulk material or more thin films with different thickness on top of a substrate. For a very precise modeling, even sample roughness or texture can be added into the model [199]. In case the bulk material is investigated, no further modeling needs to be done and the dielectric function can be obtained directly (even analytically) from the (ψ, Δ) measurement. In order to obtain the dielectric function of the specific film, dielectric functions and thicknesses of all remaining films have to be known. Besides, to be able to properly model the dielectric function, the thickness of the measured film is also required.

The dielectric function modeling is the most important part of the spectroscopic ellipsometry, which requires a lot of knowledge and skill, especially if there is a very little known about the material. It is the process during which the dielectric function is constructed using Lorentz, Drude, Cauchy, Tauc-Lorentz and many more oscillators [1]. Positions and shapes of these resonators describe electron transitions in the band struc-
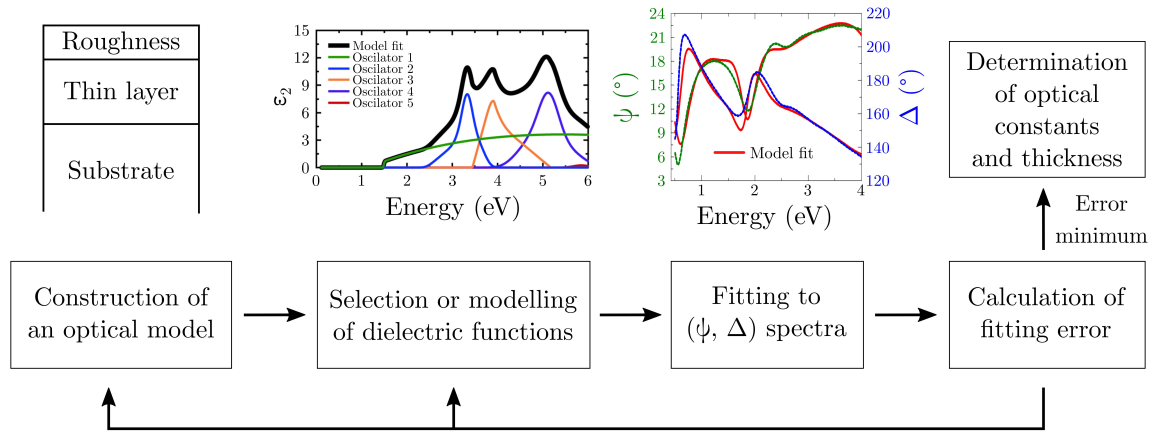
Figure 3.3: Flowchart of the ellipsometry data analysis. The first image (from left) shows an illustrative optical model of a sample formed by the thin layer with roughness, on top of a substrate. The second image (from left) represents a graph of an illustrative imaginary part of a dielectric function formed by 5 oscillators. The third image (from left) represents also a graph that displays fitting to measured (ψ,Δ) spectra. Adapted from [199].

ture of the measured film. Therefore, the selection of these resonators is what requires the above-mentioned knowledge and skill. Another difficulty is the fact that this dielectric function can not be compared directly with the ellipsometry measurement. This function represents only one input of a system, from which the (ψ,Δ) are calculated and compared with the measured (ψ,Δ) spectra.

The fitting to the measured (ψ,Δ) spectra are an inseparable part of the dielectric function modeling and represents a numerical optimization of the chosen parameters of resonators or the film thickness. By changing these parameters and comparing the measured and modeled (ψ,Δ) spectra, we are able to determine optical constants and thickness of the specific film.

3.3 Electron beam lithography

Electron beam lithography (EBL) is one of the most used processes in nanofabrication. It is used for manipulating polymer topography with nanoscale precision that serves as a mask for local doping, thin film deposition or dry etching [200, 201]. EBL process consists of three steps: spin-coating, e-beam patterning and development (Figure 3.4). The spin-coating is a process during which an electron sensitive film of a polymer resist is dispersed on top of a sample by a fast-rotating instrument called spin-coater, and subsequently tempered by a heater. The tempered resist is inserted into a lithography instrument, where some specific pattern is exposed by a scanning focused e-beam.

To expose the pattern successfully (as close to the design as possible), the e-beam parameters have to be adjusted (voltage, current, step size and area dose) for each resist and for the specific size and confinement of structures [202]. In generally, there are two types of electron sensitive resistys – positive and negative – that behave differently upon the e-beam exposure. While in the positive resist the polymer bonds tend to break, the bonds in the negative resist harden when they are exposed to the e-beam. When the sample is finally developed in prescribed chemicals characteristic for the used resist, the exposed areas on the positive resist are washed away, while on the negative resist they remain (Figure 3.4). The negative resist is used when areas that have to be covered with a material are larger than remaining areas or in case the negative resist is applied directly as a hard mask.

One significant EBL advantage, compared to other nanofabrication methods such as ion beam deposition, optical lithography, or direct laser writing, is the lateral resolution of fabricated structures [203]. This advantage is however compensated with length of the e-beam exposure, which could be very limiting in case of mass production. Nonetheless, for metasurface research purposes where only small areas of nanostructures are required, this method is perfectly suited.
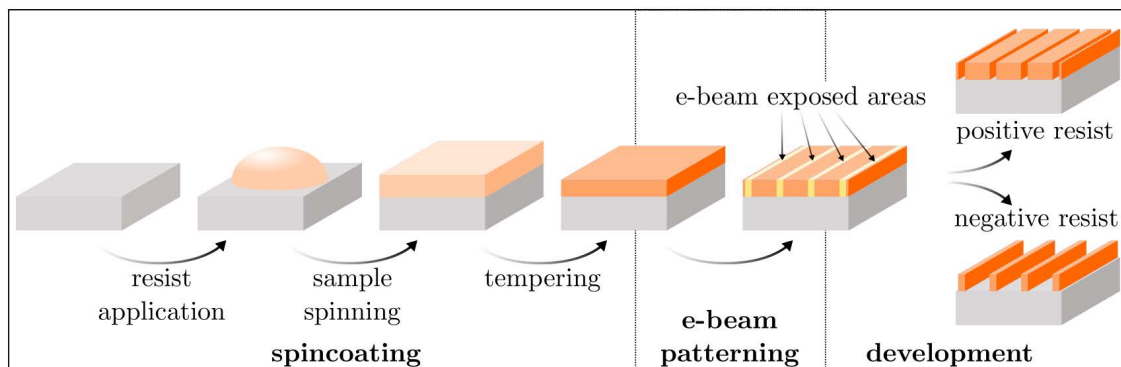

Figure 3.4: EBL process. A sample is covered with an electron sensitive resist, exposed to a focused e-beam and subsequently a polymer mask is developed in an appropriate solvent [47].

3.4 Coherence-controlled holographic microscopy

An image in regular transmissive optical microscopes is formed by interference of diffracted and direct light beams in the image plane [204]. Nonetheless, these common microscopes provide information only about the transmitted intensity [47]. To obtain information about a phase shift introduced by a sample, quantitative interference microscopy techniques, such as phase stepping interferometry (PSI) or digital holographic microscopy (DHM), have to be used. The PSI technique is based on the interference of two parallel, reference (passing through a substrate) and object (passing through a sample). Because of a number of unknown parameters, a set of 4 phase shift varying measurements must be carried out to obtain the information about the complex wave (amplitude and phase) transmitted through the sample. In this technique, low-coherence light sources can be used [204]. The DHM technique introduces spatial angle between the object and reference beams, creating a sample hologram. Due to this modification, only one measurement is sufficient to obtain the phase shift information, but at a cost of coherence light source requirement [205].

Coherence-controlled holographic microscope (CCHM), designed at Brno University of Technology, combines the aforementioned two interference microscopy techniques. While relaxing the requirement for coherence light sources, CCHM can still reconstruct

Legend: LS...light source, P...pinhole, BF...bandpass filter, RL...relay lens, BS...beam splitter, M...mirror, C...condensor, SP...specimen, RO...reference object, O...objective, TL...tube lens, OL...output lens, OP...output plane
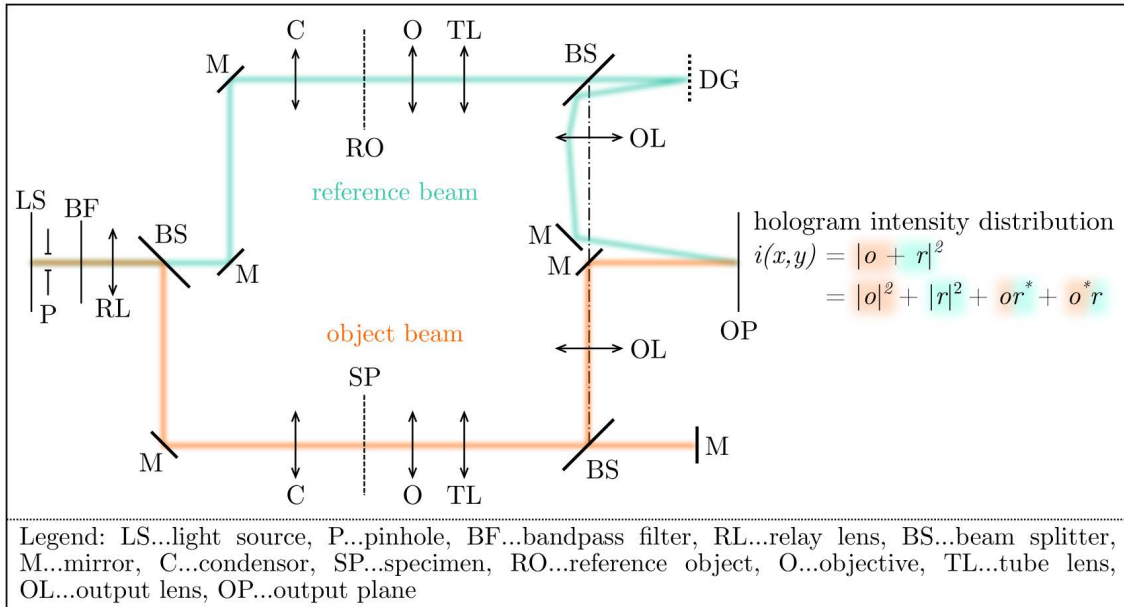
Figure 3.5: Scheme of the CCHM designed at Brno University of Technology. The parameter $i(x,y)$ represents superposition intensity of object (o) and reference (r) complex amplitudes. [47].

the sample hologram out of a single measurement. This is possible due to its specific construction (Figure 3.5), where the object beam (cyan line) passes through the sample into the output plane (CCD chip) and the reference beam (orange line) is diffracted on the specific grating and subsequently interfere with the object beam under the small angle. This interference in the image plane creates the hologram, which can be described as

$$i\left(x,y\right) = \left|o\left(x,y\right) + r\left(x,y\right)\right|^2 = \left|o\right|^2 + \left|r\right|^2 + o^*r + or^*, \qquad (3.6)$$

where $o\left(x,y\right)$ is a complex amplitude of the object beam and $r\left(x,y\right)$ is a complex amplitude of the reference beam. The first two terms on the right side of the equation represent individual intensities of the object and reference beam, respectively, and the other two terms are complex conjugates of complex amplitudes of the object and reference beam [47, 204].

To obtain the phase shift from the hologram, the following procedure has to be followed. First, a fast Fourier transformation is applied on the hologram. This creates a two-dimensional spectrum of three spatial frequencies. In the center of this spectrum is the zero-order term that corresponds to the sum of the reference and object beam intensities. The other two frequencies in this spectrum represent complex conjugates of complex amplitudes of the object and reference beam. To extract the phase shift between the object and reference beam, a reverse fast Fourier transformation of only one of those conjugates has to be carried out. The reconstructed hologram will contain frequency, which represent the phase difference between the reference and object beam. In case the specific phase quantification of each point on the sample should be measured, the reference beam must pass through the same substrate as is used for the sample. In case the area of interest is restricted and surrounded by the bare substrate, the phase difference can be obtained directly from the reconstructed image without any requirement on the reference sample. The outlined procedure might provide also information about the transmitted intensity. However, it is important to note that this transmission includes information also about the reference beam. To obtain the transmission only through the specific area of interest, it is better to use simple transmission optical spectroscopy. This way we can obtain both transmission phase and amplitude information of any area of interest.

4. Results

After having discussed how to construct a metasurface and how VO_2 works, the final chapter of this thesis focuses on implementing pure VO_2 nanostructures into a tunable metasurface. The first part of this chapter is dedicated to optimization of VO_2 thin film deposition, which is crucial for all subsequent steps. Dielectric function, obtained from the VO_2 thin film with the largest FOM, is used in the second section for metasurface building block simulations. The most promising VO_2 building block library is chosen by comparing influences of height, spacing and wavelength. Building blocks are then fabricated and their measured optical response is compared with simulations. The last part of this chapter is devoted to a tunable metasurface transmission filter, on which the possibility of optical tuning is demonstrated.

4.1 Thin film optimization

For any type of metasurface, it is necessary to be able to fabricate a high quality thin film of a certain material first. Especially VO_2, as we could see in the Section 2.2, requires very careful optimization. Hence, in this section we will describe our process of VO_2 optimization. VO_2 is deposited by e-beam evaporation system with a post-annealing in a vacuum furnace. We decided to use this combination for its deposition speed and possibility of fabricating a bigger amount of samples at once. The quality of VO_2 films was evaluated by FOM (Eq. 2.1) and by transmission spectra obtained from spectroscopic ellipsometry or from transmission spectroscopy, respectively.

The whole VO_2 thin film fabrication process started with preparation of 10×10 mm silicon (Si) and fused silica (SiO_2) substrates, which were cut from 4 inch wafer (Siegert, intrinsic, <100>, >10 kΩ cm, 252±20 μm, DSP) by Oxford Lasers' laser dicer. Subsequently, the samples were cleaned for 2 min in acetone, 2 min in isopropyl alcohol (IPA) and 30 s in deionized (DI) water, applying an ultrasound treatment the whole time. To get rid of water residuals before the deposition, the samples were (soft) baked for 2 min on a 150 °C heat plate. Then all the samples were immediately taped onto the evapo-

ration sample holder and inserted into the evaporation vacuum chamber to keep air and dust contamination at minimum. We experienced that some VO_2 thin films where substrates were not cleaned right before the deposition exhibited lower adhesion. Even though this influence was not properly examined, we advice to always clean samples right before the deposition. Note that some samples were partially covered with the tape, to create a protected area with respect to which the thickness can be measured by a mechanical profilometer after the deposition.

The thin film was deposited by evaporating VO_2 powder (Mateck, purity $98+\%$, mesh $\leq 500\,\mu$m) in Bestec's e-beam evaporator at $6\,$kV and 40–$50\,$mA. Already at these conditions, VO_2 powder evaporated so quickly that the focused e-beam was creating holes in the powder, lowering the deposition rate. To get as homogeneous film as possible, we wanted to keep the deposition rate during the whole time stable at $1\,\text{Å}\,\text{s}^{-1}$. Moving the whole focused beam into a different place in the crucible would result in sudden increase in the deposition rate. Therefore, the current had to be continuously adjusted to keep the deposition rate at $1\,\text{Å}\,\text{s}^{-1}$. The desired thickness of the film was set to $200\,$nm and it was controlled by an in-situ thickness meter, compensated with a $64\,\%$ tooling factor. To ensure the thickness is same over the whole sample area, the sample holder was rotating at $5\,$rpm.

After the deposition, the thickness was verified by the mechanical profilometer Bruker Dektak XT. We found out that the actual thickness of thin films was $260\pm15\,$nm. We therefore concluded that the tooling factor has to be adjusted for future depositions. A transmission measurement of the deposited thin films performed below and above VO_2 phase-transition temperature (Figure 4.1a) confirmed our assumption that the deposition environment without controlled temperature and oxygen atmosphere will not result in the stoichiometric VO_2 thin film exhibiting the phase-transition. A subsequent XPS measurement of these films (Figure 4.1b) showed that they consisted mostly of two oxidation states, where the oxidation state V^{5+} representing V_2O_5, was contained more than V^{4+} representing VO_2. Unfortunately, the electron beam in our evaporation system is emitted by a heated tungsten filament, so the oxygen can not be injected into this system. Due to this reason, the post-annealing process in the vacuum furnace was added after the deposition. The optimization process started at this point, where we separately tested annealing temperatures and oxygen flows at fixed $10\,$min annealing time, $2 \times 10^{-10}\,$mbar base pressure, $20\,°\text{C}\,\text{s}^{-1}$ heating rate and free-cooling. The fixed parameters were chosen based on literature and instrument possibilities, to keep only two optimized parameters.
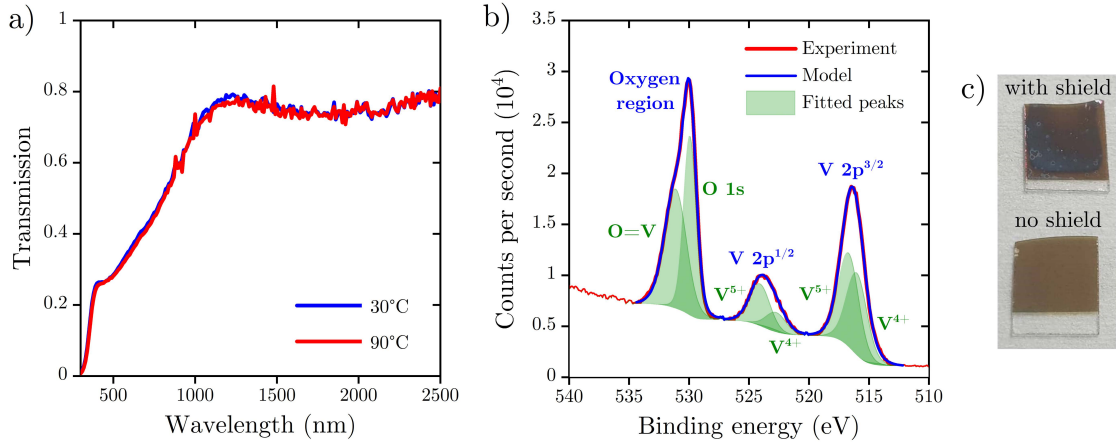
Figure 4.1: a) Transmission spectra of the VO$_2$ thin film as deposited by e-beam evaporation, measured at 30 °C and 90 °C. b) Measured (red line) and modelled (blue line) XPS spectrum of the deposited VO$_2$ thin film. The modelled spectrum consists of three regions that are formed by separate peaks (green areas) which correspond to the specific oxidation state listed in the graph. c) Photographs of two samples after annealing at same parameters, but with or without the protective shield between the lid and the sample.

We started with the a oxygen flow under 15 sccm and tested temperatures ranging from 400 °C to 600 °C, with a 50 °C step. We annealed one film on Si substrate and one film on SiO$_2$ substrate simultaneously at each of the five annealing temperatures. Two substrate materials were required as we aimed for transmissive applications in the VIS region (hence SiO$_2$ substrate), but spectroscopic ellipsometry is problematic on transparent substrates (hence Si substrate). The samples were inserted precisely 27 cm from the tube opening. A protective shield that is placed between gas inlets and the samples was removed. We found that keeping the same sample position and removing the shield is very important as previous processes showed that temperature might vary within the tube and that the heated shield can react with the oxygen flow and contaminate the sample (see Figure 4.1c). All Si substrate samples, annealed at five different temperatures, were measured by spectroscopic ellipsometry. The dielectric functions of both VO$_2$ phases were obtained by the process described in Section 3.2. For the temperature control in all spectroscopic experiments we used a feedback-controlled heating stage, which included a resistive heater and a thermocouple. We found out that the dielectric function of VO$_2$ dielectric phase could be adequately modelled by two Lorentz oscillators, and the dielectric function of VO$_2$ metallic phase was represented by one Lorentz oscillator and a Drude term. The fitting process also resulted in a deviation from the thickness measured before annealing (260±15 nm), towards the thickness estimate of 190 nm. This difference could be caused by alteration of the

film structural composition during the annealing, or by its partial evaporation at the elevated temperature. This discrepancy indicates that the thickness has to be measured also after the annealing. By calculating FOM spectra using Eq. 2.1 we found that all annealed films exhibited the desired phase-transition (Figure 4.2a). As the film annealed at 450 °C exhibited the largest FOM, the subsequent annealing optimization of oxygen flow was carried out at 450 °C.

Following the same procedure but with the fixed 450 °C annealing temperature, we tested various oxygen flow rates ranging from 5 sccm to 25 sccm, with a 5 sccm step. The highest flow rate has been limited to 25 sccm, because higher values would cause excessive stress to our turbomolecular pump. Calculated FOMs in Figure 4.2b prove that all annealed samples exhibited the phase-transition. The sample annealed under 15 sccm oxygen flow exhibited again the largest FOM. By comparing Figure 4.2a and Figure 4.2b, we can infer that at least in our case, the VO$_2$'s FOM is more sensitive to the varying oxygen flow than to the varying annealing temperature. To conclude, VO$_2$ thin film with 190 nm thickness exhibits the biggest refractive index difference with the lowest absorption coefficient when annealed after e-beam evaporation for 10 min at 450 °C under 15 sccm oxygen flow.

A large drawback of the FOM metric is the amount of time and work required for the spectroscopic ellipsometry measurement and analysis of each sample. To speed up the optimization process on can use only transmission spectra acquired from the dielectric phase of VO$_2$ on a transparent substrate. In Figure 4.2c we compare transmission spectra at 30 °C of samples annealed under 15 sccm oxygen flow and temperatures listed in the graph. We can see that relative positions of transmission spectra of different annealing temperatures are similar to the relative positions of FOM in Figure 4.2a.
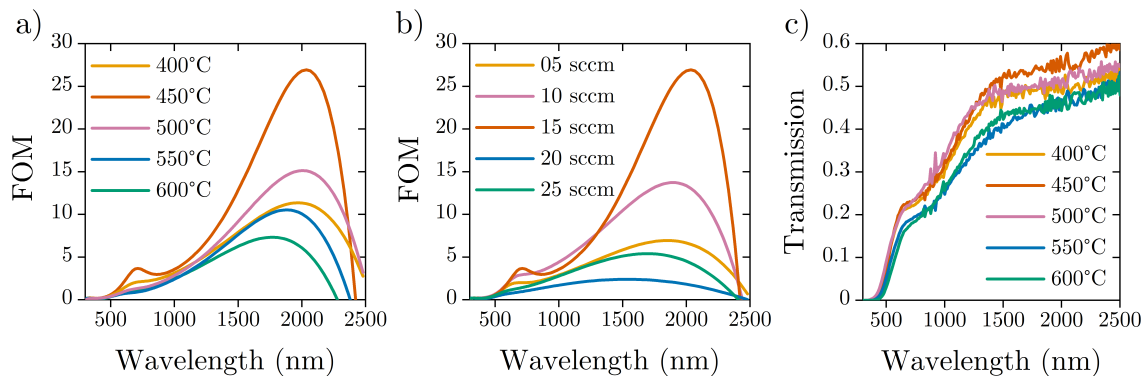

Figure 4.2: FOM spectra of samples annealed for 10 min a) under 15 sccm oxygen flow at the temperatures listed in the graph, and b) at 450 °C under the oxygen flows listed in the graph. c) Room-temperature transmission spectra of a 190 nm VO$_2$ film on SiO$_2$ substrate, annealed under 15 sccm oxygen flow at the temperatures listed in the graph.

This similarity arises from the fact that transmission spectra are mostly lowered by the increasing absorption coefficient, which represents the denominator in the FOM metric. It is important to note that transmission spectra are measured on samples with SiO_2 substrates, while FOM is calculated from the dielectric function obtained from samples on Si substrates. The similarity of relative positions therefore supports also our assumption that the dielectric function of VO_2 is insensitive to the substrate. However, transmission spectra can be used as a proxy for FOM only in case the thickness of the VO_2 film is similar or lower than 200 nm. Due to absorbing nature of VO_2 thicker films would result in very low transmission. Then the noise of the measurement could influence this method more significantly.

We close this section with a comparison of our optimized VO_2 film with films in the library from Section 2.2. In Figure 4.3a we can see that FOM of our optimized VO_2 film is either comparable or even better than other films reported in the literature. We ascribe this fact to a very low absorption coefficient in our VO_2's dielectric phase (Figure 4.3c). Despite the fact that our model of the dielectric function might be imperfect and that extraction of complex refractive indices from the literature has also some error, we are able to fabricate a low-loss VO_2 film (Figure 4.3c) with large optical modulation in the VIS and NIR region (Figure 4.3b).

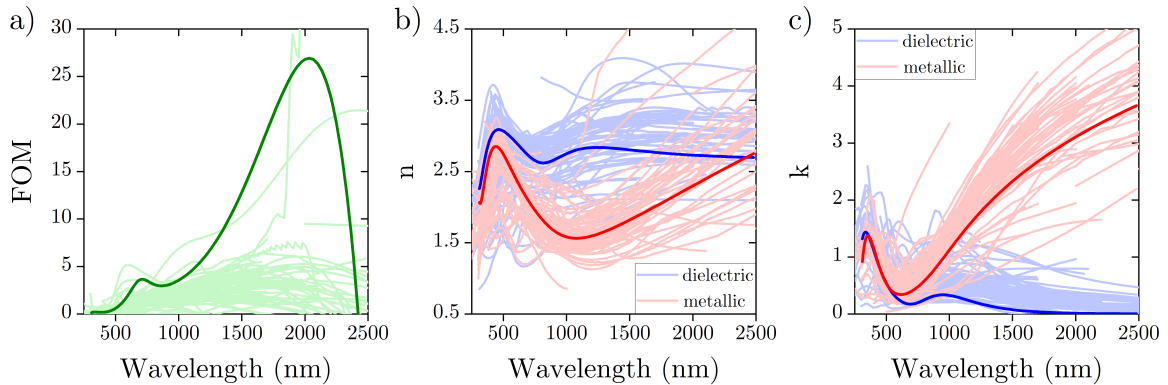**Figure 4.3:** a) FOM spectra of our optimized 190 nm VO_2 film on Si (thick green line) in contrast to library of FOMs (light green lines) [80, 81, 99–177]. b) Refractive index and c) absorption coefficient of our optimized 190 nm VO_2 film in its dielectric (thick blue line) and metallic (thick red line) phase, in contrast to library of refractive indices and absorption coefficients extracted from.

4.2   Metasurface building blocks

Any metasurface is made of building blocks (referred as only blocks below), which are responsible for the specific amplitude, phase, and polarization control. While most of practical metasurfaces require at least 2π phase coverage of its blocks, there are some that are based only on the control of a light amplitude. These amplitude metasurfaces are mostly formed by blocks that exhibit a certain plasmonic or dielectric resonance [206]. To determine the type of a metasurface, we must look at its block libraries. In most transmissive metasurface applications, block libraries (the transmission phase and amplitude as functions of a block size or rotation) are obtained from simulations, in which the dielectric function of the actual deposited material is used [8]. While simulations of transmission are easily verified experimentally, the phase is due to specialized instrumentation measured rarely [47]. Because VO_2 might be affected by many influences during the nanostructuring process, experimental verification could be useful, however. Fortunately, we have opportunity to use such specialized instrument for the phase measurement at our institute.

In the following section we will firstly create a simulated block library using the refractive index of the optimized $190\,nm$ VO_2 film (see Section 4.1). As our prime focus is the visible region, where VO_2 has still relatively high absorption, we will have to search for the library with the lowest absorption and full 2π phase coverage. We will do so, by comparing different physical properties, such as a wavelength, height and spacing between blocks. After obtaining the optimal block parameters, we will try to fabricate them and measure their transmission phase and amplitude.

The word *phase* in this section might become confusing, as it is used for both, the phase shift of the light wave and the phase-transition of the VO_2. We will therefore reserve this word for the light's phase shift and the word phase-transition will be replaced by a *form* or *structural* transition.

4.2.1   Simulations

In Figure 1.3 we could see that a building block library can be represented by a graph, in which the transmission phase and amplitude are functions of the block's size (in case of propagation-phase) or rotation (in case of geometrical phase). These functions depend not only on the size or rotation, however, but also on the block's height, shape, spacing between the blocks, and on the used wavelength. Most of these parameters are often referred to as "degrees of freedom" in this context [207]. Dependency on the size

or rotation is often described in the library as these parameters are the easiest ones to be both simulated and then controlled during the fabrication. Materials such as VO_2 add another degree of freedom by means of their structural transition. To examine the change of the phase and amplitude during the VO_2 transition, we will simulate pure propagation-phase VO_2 blocks, with a polarization-insensitive cylindrical shape.

Simulations were carried out using the finite-difference time-domain (FDTD) method in the Lumerical FDTD Solutions software. The distance between the nanocylinders and the vertical FDTD region boundary was always kept at least a half of the longest recorded wavelength. Conformal meshing (mesh order 4) was adopted everywhere except the VO_2 nanocylinders, where we opted for staircase meshing with a 5 nm step. To have physically more correct solution. We chose to simulate a finite array of 5×5 nanocylinders (Figure 4.4) rather than periodic lateral boundary conditions to obtain more practically relevant solutions. This number of nanocylinders in the array was the optimal choice exhibiting the characteristic finite lattice effect while keeping the memory and time requirements reasonably low. Simulations employed a total-field scattered-field (TFSF) source with appropriate symmetry conditions and perfectly matched layers (PML) boundary conditions. To incorporate the lattice effect, TFSF source was applied only on the middle nanocylinder, while the polarization currents induced within the each nanocylinder were recorded. The procedure for calculation of the transmitted far-field phase and amplitude consisted of a subsequent employment of the Green's function formalism [14], which was incorporated in the post-processing Matlab script provided by our colleague Martin Hrtoň.
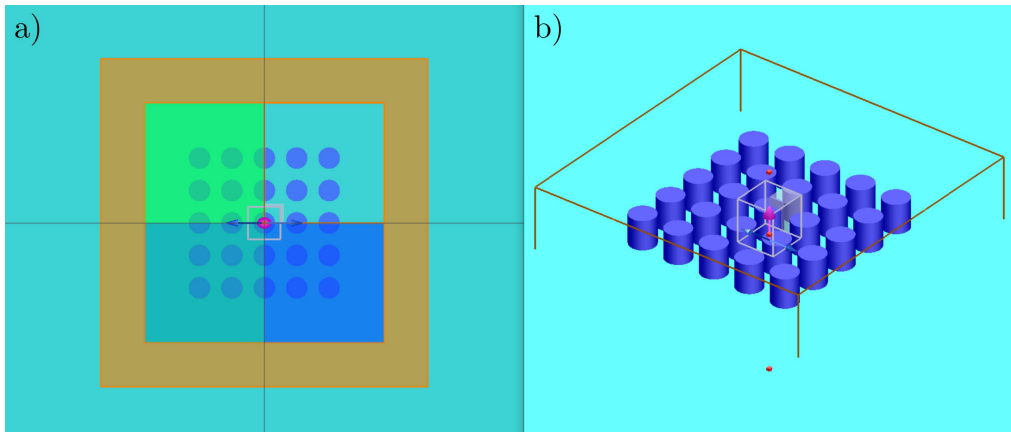
Figure 4.4: a) Top and b) perspective view of the simulated 5×5 VO_2 nanocylinder array (dark blue) on the SiO_2 substrate (light blue background). Orange square in a) is the boundary of the simulated area, with anti-symmetric (green) and symmetric (blue) boundary conditions. The grey square in the middle of both views represents the TFSF source with an electric field aligned along x axis (blue arrow) and propagating along positive z direction (pink arrow).

The first set of simulations was focused on the influence of the cylinder's height on the transmitted phase and amplitude. The spacing between centers of nanocylinders was fixed at 300 nm. The 680 nm wavelength was chosen based on relatively low absorption in the VIS region (Figure 4.3c) and based on possibilities of subsequent experimental verification. In Figure 4.5 there are 6 graphs, representing 6 different heights (H), in which the phase and amplitude (in the form of transmission intensity) are represented as functions of the nanocylinder diameters in both VO_2 forms. The first thing we can see is very similar transmission behavior no matter whether the VO_2 is in the dielectric or metallic form. This behavior results from their very similar absorption coefficients in the VIS region (Figure 4.3c). The absorbing nature of VO_2 is also responsible for generally low transmission through the nanocylinders. With the increasing height and therefore with an increasing amount of material, this absorption is pronounced even more. Nonetheless, the increased height means also a longer propagation path of light, which produces the increased phase shift. Nanocylinders in the dielectric form with heights above 500 nm cover the full 2π phase shift over the available blocks. As such coverage is required for a properly functional metasurface, the VO_2 blocks have to be with high aspect ratio despite their absorbing nature.

Figure 4.5: Simulated phase (full line, left axes) and transmission (dashed line, right axes) of VO_2 nanocylinders in the dielectric (blue) and metallic (red) form as functions of diameters. Each graph represents simulations for the height listed above the graph. The spacing is fixed to 300 nm and the wavelength is 680 nm.

While the transmission during the VO$_2$ transition stayed almost unchanged, the phase shift of the biggest blocks changed almost by π. This proves a possibility to encode the phase information into different forms of VO$_2$, where we could for example use only the block with one diameter, and change its phase shift by the temperature or by the optical power.

To investigate if this tunability and the transmitted intensity can be improved, we carried out a second set of simulations, where we kept the fixed 500 nm height, 680 nm wavelength and varied the block spacing. In Figure 4.6 we can see 4 graphs representing 4 different spacings (S), which were chosen based on fabrication possibilities (limiting the lowest value) and based on an assumed range of block's interactions (limiting the highest value). It is important to note that the bigger spacing enables bigger diameters, therefore x-axes vary for different spacings. We can observe that transmissions of both VO$_2$ forms are no longer similar when spacing is different than 300 nm. Specifically, with the increasing spacing we can observe that the transmitted intensity of the dielectric VO$_2$ nanocylinders experiences a sudden decrease around 200 nm diameter. This decrease in transmission is accompanied by a significant jump in the phase. Such
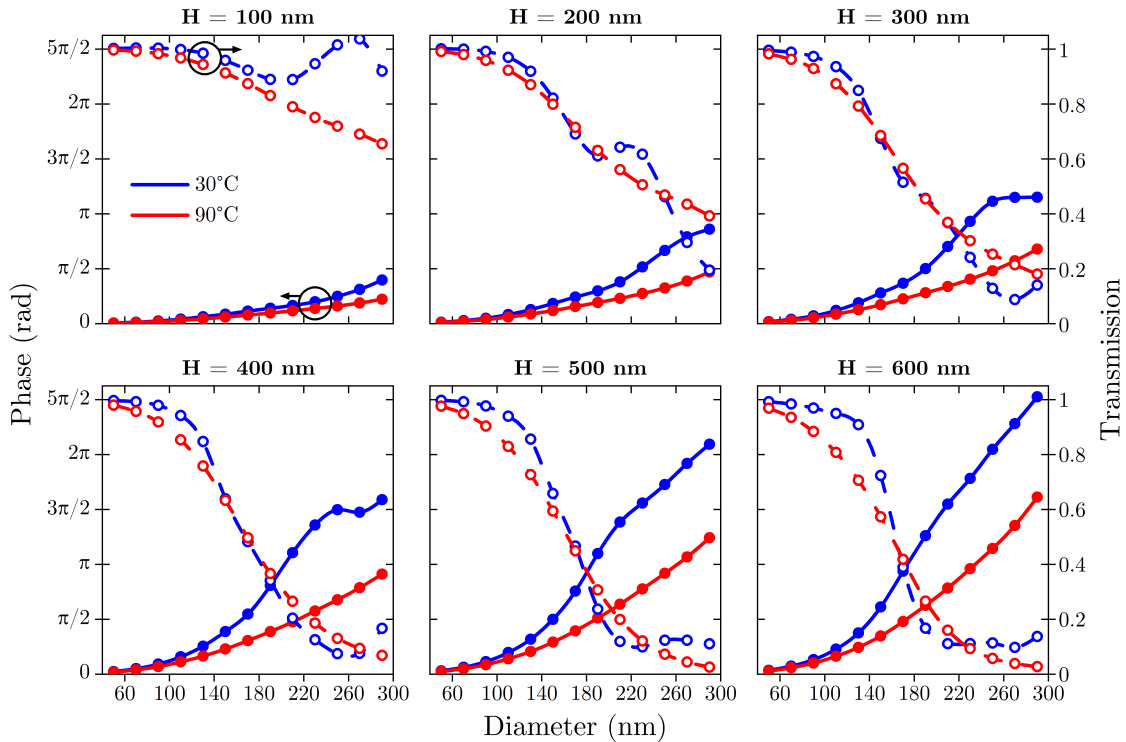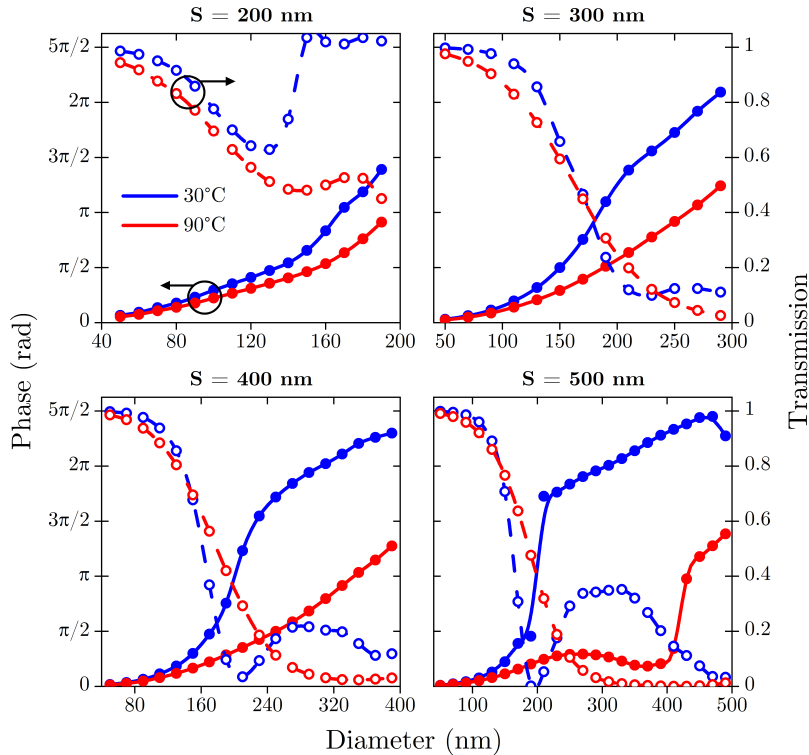

Figure 4.6: Simulated phase (full line, left axes) and transmission (dashed line, right axes) of VO$_2$ nanocylinders in the dielectric (blue) and metallic (red) form as functions of diameters. Each graph represents simulations for the spacing listed above the graph. The height is fixed to 500 nm and the wavelength is 680 nm.

behavior can be understood from the lattice effect of dielectric Mie resonances that occur in VO$_2$ structures [206, 208]. Note that resonances can be also found in lower nanocylinders (less than 500 nm), but the increase in the phase is not so strong due to resonances being suppressed by the absorption. The transmission through the metallic VO$_2$ nanocylinders with diameters above 300 nm is almost zero for all possible spacings. Such behaviour restricts VO$_2$ metasurfaces in the VIS only to metasurfaces that can be switched on and off, as the efficiency of these metasurfaces is very poor in the metallic form. The sudden change in the phase that is most pronounced for the 500 nm spacing is usually undesired in regular metasurfaces where the phase continuously depends on the block diameter. However, in VO$_2$ metasurfaces where we look at the change of the phase during the VO$_2$ transition, it can be exploited. For example, the sudden increase of the phase for blocks with 500 nm spacing leads to almost $3/2\pi$ difference between the dielectric and metallic form of a 230 nm diameter nanocylinder, while transmission stays unchanged at 20 %. This effect can be used for the tunable metasurfaces which can be gradually tuned between two forms, encoding various phase information. The full understanding of the spacing influence on the block properties would require deeper investigation of the lattice resonances that is beyond the scope of this thesis.

In the third set of simulations we wanted to see what happens when light of different wavelengths is used. We kept the fixed 300 nm spacing and 500 nm height. In Figure 4.7 we can see 3 graphs representing 3 different wavelengths (W), which were chosen based on a standard wavelength of a red laser (lower value) and based on a limit of the VIS region (higher value). With the decreasing wavelength we can observe that transmission of smaller blocks also decreases. It is the result of an increasing absorption coefficient in smaller wavelengths (Figure 4.3c). Nonetheless, the light with smaller wavelength is phase shifted more (see Equation 1.2), resulting in the bigger phase. As the absorption of VO$_2$ decreases almost to zero in the NIR region, we could be able to obtain tunable building blocks in the NIR region that cover the whole 2π phase shift with a very high transmission. This opens up the possibility for further research in the future, but in the current work we are focused on the visible part of spectrum only.

To sum up this section, we could see that not only the size of the propagation block influences its transmission phase and amplitude, but also its height, spacing and the used wavelength. Focusing on nanocylinders and specifically on their height, we found that for a properly functional metasurface, nanocylinders have to be at least 500 nm high. When operating at 680 nm wavelength, nanocylinders with this height represented also the best balance between the transmission phase (2π) and amplitude (10 %) and exhibited interesting behaviour of nanocylinders with different center-to-center spacings.
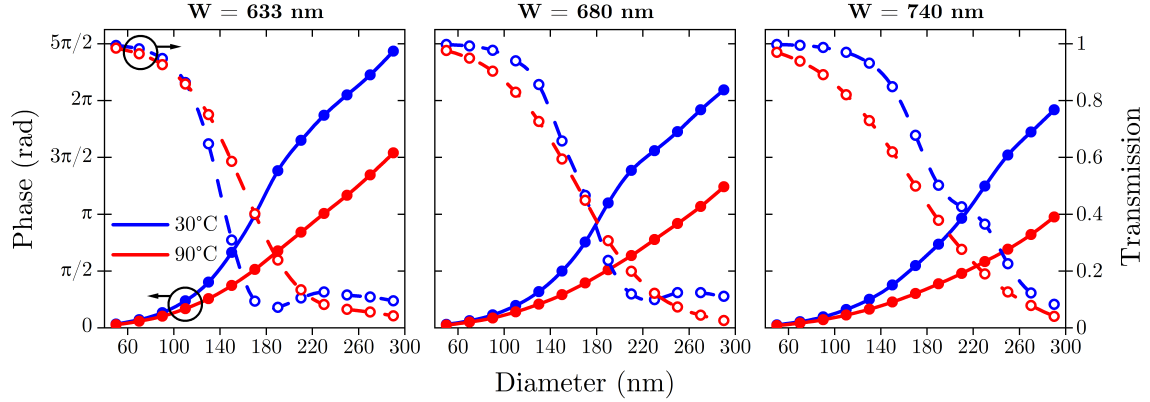
Figure 4.7: Simulated phase (full line, left axes) and transmission (dashed line, right axes) of VO$_2$ nanocylinders in the dielectric (blue) and metallic (red) form as functions of diameters. Each graph represents simulations for the wavelength listed above the graph. The height is fixed to 500 nm and the spacing is 300 nm.

4.2.2 Fabrication

Simulations have shown us that despite the occurring Mie resonances, pure VO$_2$ metasurfaces in the visible based on the propagation-phase can be functional only when high aspect ratio blocks are used. That means more than 500 nm height of building blocks. Such high blocks are mostly produced by firstly fabricating the thin film with the thickness equal to the final height of blocks and subsequently etching the undesired material through a lithographically prepared mask [47]. We therefore deposited a 560 nm film of a non-stoichiometric VO$_2$ using e-beam evaporation. The 560 nm was chosen as we accounted for some material reduction during the annealing process (see Section 4.1). We then annealed the sample using the optimized parameters. We expected that the quality of this VO$_2$ film might be different than the quality of the 190 nm film discussed in Section 4.1, as the amount of material to be oxidized was significantly bigger. To our surprise, we observed no transition. Even by changing some of the annealing parameters we were still not able to produce a VO$_2$ film exhibiting the desired transition. This complication only proved the delicacy of the VO$_2$ fabrication process. As a completely new optimization process with a search for the cause of this problem would be very time consuming, we decided to try a different approach:

The other approach was based on annealing of the already fabricated blocks. The non-stoichiometric blocks were created by EBL and e-beam evaporation first, and they were annealed using the optimized parameters afterward. This way, only the smaller amount of the material blocks had to be oxidized and not the whole film, which could result in VO$_2$ with the proper transition.

The fabrication started with substrate cleaning procedure, which was the same as for the thin film optimization (Section 4.1). The cleaned SiO_2 samples were spin-coated with the positive e-beam resist AR-P 6200.13 and the protective coating AR-PC 5090.04 (both from Allresist GmbH). For the spin-coating and tempering we followed their respective datasheets. Samples were then inserted into SEM Mira 3 (TESCAN) with a lithographic stage system (from RAITH). Using 30 kV voltage, 25 pA beam current, 5 nm step size and 120 µC cm^{-2} dose factor, we exposed 100×100 µm nanocylinder arrays. Center-to-center spacings between nanocylinders ranged from 200 nm to 500 nm, and nanocylinder diameters were from 100 nm to the size which was 10 nm smaller than the specific spacing. After the exposed resist mask was developed, we deposited 393 nm of non-stoichiometric non-stoichiometric using e-beam evaporation. After the deposition, the residual resist was removed during the lift-off process, leaving the resulting nanocylinders on top of the substrate. We deposited only 393 nm instead of the planned 560 nm because we were limited by the maximum resist thickness. Thicker resists could solve this problem, but the achievable lateral resolution would decrease. This would mean that most of the nanocylinders would not be fabricated. Lowering the deposited thickness allowed to fabricate nanocylinders with smaller diameters.

After the deposition we measured the height, shape, and diameter of nanocylinders with 500 nm spacing to have a reference on what and how was affected by the subsequent annealing process. The height and shape was measured using scanning probe microscope (SPM) Icon, from Bruker Dimension company. Nanocylinder diameters were extracted from SEM micrographs, as due to noise it was harder to obtain them from SPM images. In Figure 4.8a, b we can see that instead of nanocylinders we ended up with nanocones or truncated nanocones. This undesired effect is related to the evaporation process, as the evaporated material is often deposited also on the edge of the resist holes and clogs them. This results in less material being evaporated in the later stages, leading to formation of the characteristic nanocones [197]. In case the diameter was large enough, the hole was not clogged completely and the nanocone became truncated. This is something we can see also in Figure 4.8c of the measured heights. Firstly, all nanocones did not have the same height, as it was always connected to the specific diameter. Secondly, nanocones above 350 nm in diameters became truncated as they were not fully clogged during the deposition and reached the deposited film thickness. In Figure 4.8d we can see the diameters measured at the bottom of nanocones as a function of the designed diameters. It shows that due to the proximity effect [209], structures under 240 nm in diameter had smaller bases than designed and structures above that value had larger bases. This means that we have to either adapt lithographic parameters or count with such non-linear dependency.

48

After reference measurements we annealed the sample using the optimized parameters (Section 4.1). As shown in Figure 4.8c, d, we can observe the reduction of heights and diameters. While the heights decreased almost by 7%, the diameters decreased only by 3%. This difference can be explained by atomic forces between the substrate and nanocones [180]. These results show that VO_2 structures are reduced similarly to the VO_2 thin film. The important factor which has to be considered in case of fabricating such VO_2 nanocones is the ratio between the height and diameter, which ended up being around 1. Combining this factor with the change of the block's shape during the evaporation process, we can conclude that instead of nanocylinders we are able to fabricate only VO_2 nanocones with the height being limited to the diameter of their base. Based on simulations from Section 4.2.1 we can say that the phase of the nanocones with such varying heights is insufficient for a properly functional metasurface. No matter how insufficient, we still can use these nanocones to experimentally verify the simulations.
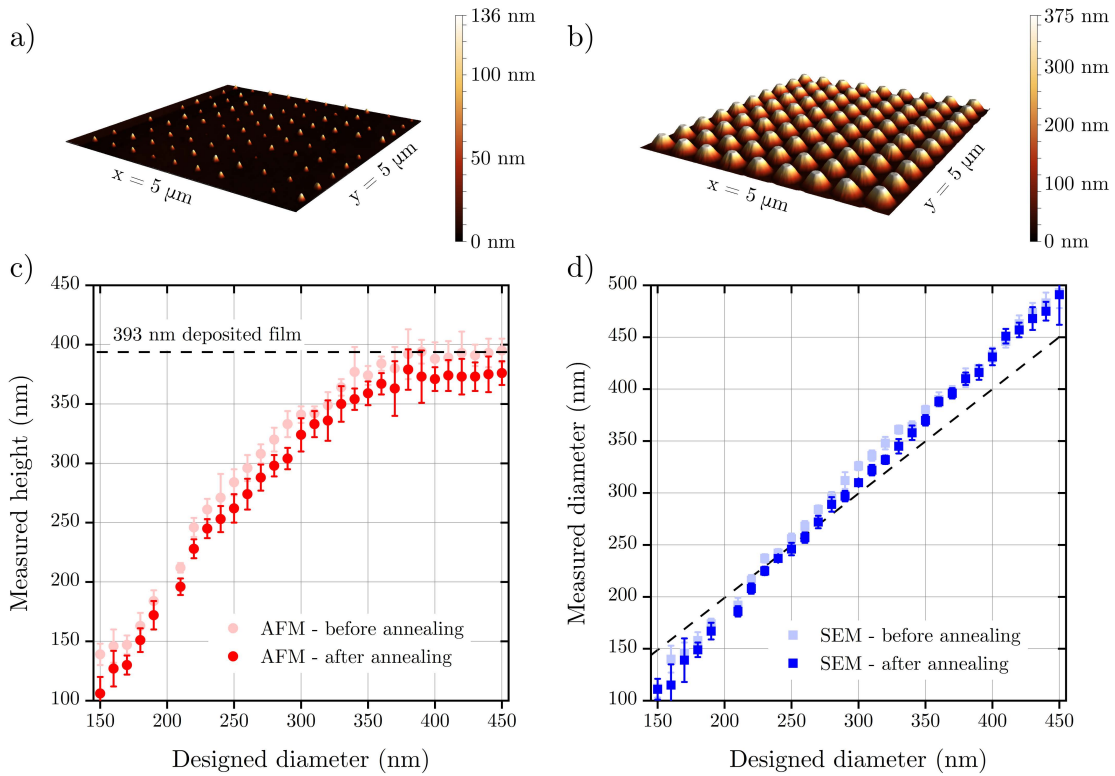
Figure 4.8: SPM topography of VO_2 a) nanocone arrays with 150 nm designed diameters and b) truncated nanocone arrays with 450 nm designed diameters. The spacing is 500 nm. The thickness of the deposited film was 393 nm. c) Height measured by SPM as a function of designed diameters before and after the VO_2 annealing. The dashed line represents the thickness of the deposited film. c) Diameters measured by SEM as a function of designed diameters before and after the VO_2 annealing. Dashed line represents an ideal case of measured and designed diameters being equal.

4.2.3   Phase measurement

Our simulations showed that nanocylinders with 500 nm height exhibit interesting transmission phase and amplitude that could be utilized into a tunable metasurface. Despite the fact that our fabricated blocks were nanocones or truncated nanocones with heights equal to their base diameters, we still found interesting to verify our simulations in experiment with such structures.

The transmitted phase was measured on CCHM by Miroslav Ďuriš, where we used a light source with 680 nm wavelength and followed the procedure described in the Section 3.4. The transmission spectra was measured on Nanonics Imaging MV 4000 optical microscope from 400 nm to 900 nm wavelength. The specific transmission amplitude at 680 nm was then extracted for each diameter in both VO_2 forms. The temperature for measuring both VO_2 forms was controlled by our feedback-controlled heating stage with a hole in the center to allow for the transmission. Simulations of the transmission phase and amplitude were carried out the same way as in the Section 4.2.1, but with the actual measured shapes and sizes of the conical blocks.

In Figure 4.9 we can see that our experimental results match the simulated ones very well. The significant oscillation in the simulated transmission phase and amplitude of the dielectric VO_2 form results from the above-mentioned Mie resonances enhanced by the lattice effect. We do not observe such resonant shape in the experimental data, as the nanocones were most probably oxidized differently than the thin film. Moreover, fabrication imperfections and limited instrument sensitivity could also influence the phase measurement. We can also observe that both experiment and simulation do not exhibit the phase shift that could be sufficient for any kind of a practical metasurface that requires the 2π phase coverage. Measuring or simulating the transmission phase and amplitude of differently spaced nanocones resulted also in the insufficient phase (not shown). We can therefore conclude that we succeeded to partially confirm the validity of our propagation block simulations, but due to difficulty with deposition and fabrication we were not able to fabricate the nanocylinders with the phase being sufficient for the practical metasurface. However, there is the other group of metasurfaces that is based purely on amplitude. In such metasurfaces we can improve the optical properties of a surface despite the insufficient propagation phase. In the following section we show that we produced such amplitude based tunable metasurface by utilizing the above-mentioned dielectric Mie resonances in VO_2 nanocones.
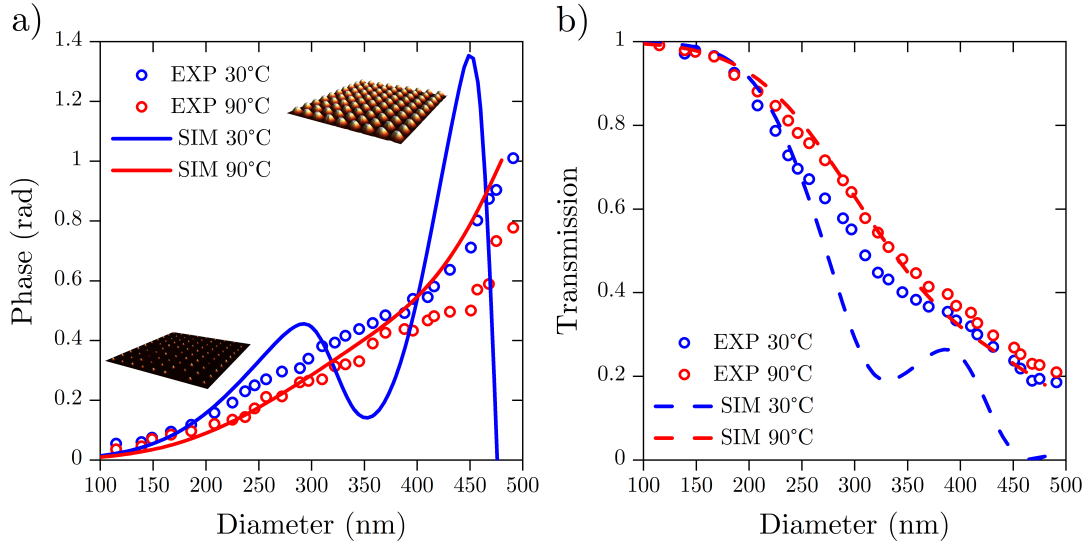
Figure 4.9: a) Phase as a function of the base diameter of conical blocks. Measured by CCHM (circles) and simulated (full line) for dielectric (blue) and metallic (red) VO_2 form. Insets represent 3D SPM images of the smallest and biggest diameter VO_2 nanocone arrays. b) Transmission as a function of the base diameter of conical blocks. Measured by Nanonics microscope (circles) and simulated (dashed line) for dielectric (blue) and metallic (red) VO_2 form.

4.3 Optically tunable transmission filter

In the final part of this thesis we will show some of our recently published results, which describe and implement dielectric Mie resonances in VO_2 nanocones into optically tunable metasurface in the VIS region [206]. Specifically, we will investigate transmission of light through the metasurface that is based only on the control of amplitude by arrays of VO_2 nanocones in both VO_2 forms. By implementing a visible laser for gradual heating and tuning of one specific array, we will demonstrate an optically tunable filter.

The nanocone arrays on SiO_2 substrate were fabricated using the same procedure as in Section 4.2.2, but instead of 393 nm height and fixed center-to-center spacing they had 200 nm height and spacing being 1.5 multiple of the base diameter. These values were chosen based on prior simulations, which showed that these type of nanocones exhibit dielectric Mie resonances in the VIS region. As the height was only 200 nm and diameters ranged from 148 nm to 300 nm, nanocones were mostly truncated. The fabricated samples were measured by transmission spectroscopy on a confocal microscopy system Witec alpha300 RA, where the sample was illuminated by a 60× NA = 0.8 objective and the transmitted light was detected by a 10× NA = 0.25 objective.

Using this setup, we observed very sharp dips in transmission spectra of VO_2 nanocones in the dielectric form, which red-shifted with the increasing nanocone diameter (Figure 4.10a). Such dips have resulted from the dielectric Mie resonances in VO_2 nanocones, specifically the electric dipole and quadrupole ones. Their narrow linewidth was caused by the lattice effect of the array [206]. When the sample was heated up, the transmission at the position of this dipolar resonance increased significantly. It was caused by decline and blue-shift of the resonance. Such behavior showed that VO_2 nanostructures in the metallic form exhibit besides plasmonic resonances (above 1100 nm wavelength [206]) also dielectric Mie resonances.

To quantify increase of the transmission, we used so-called transmission modulation depth, defined as $10\log(T_{90\,°C}/T_{30\,°C})$, where $T_{30\,°C}$ and $T_{90\,°C}$ represent intensity transmitted through the nanocone array, measured at 30 °C and 90 °C, respectively. In Figure 4.10b we can see spectra of the transmission modulation depth, calculated from the transmission measured through the nanocone arrays. We can observe two interesting phenomena. The first phenomenon is the large modulation depth that exceeded 5 dB, a value generally considered challenging to achieve with state-of-the-art tunable metasurfaces [210]. The second phenomenon is the narrow linewidth of these modulations (full width at half maximum up to 77 nm), which results in encoding the modulation depth at a selected wavelength into the specific diameter of the nanocone. Such property can be used in metasurfaces with spatially varying transmission modulation of units of decibels associated with the externally controlled VO_2 transition.
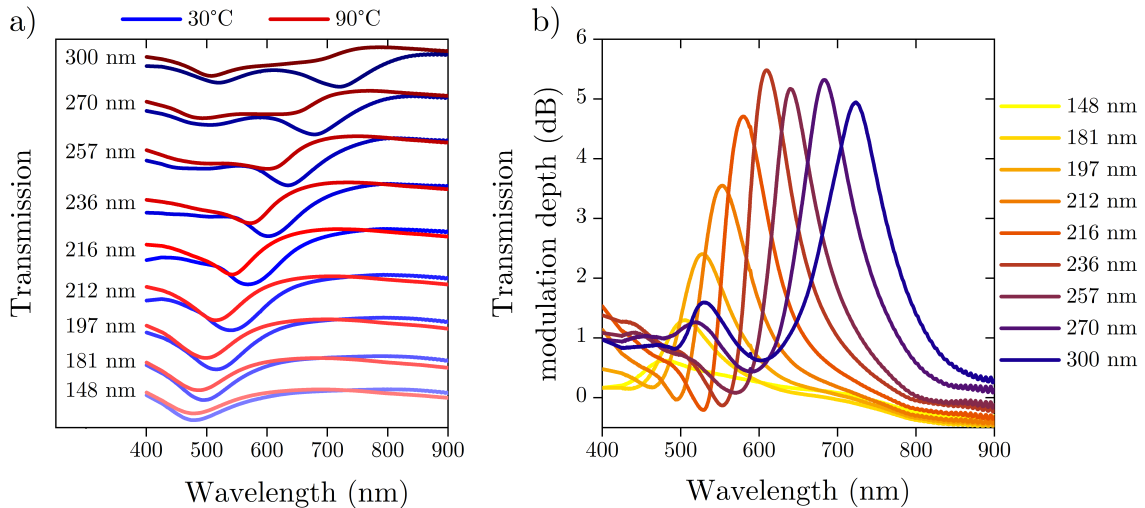

Figure 4.10: a) Transmission spectra of VO_2 nanocone arrays with 200 nm height, 1.5D spacing and diameters listed in the graph. Spectra of different diameters are stacked by a constant value for a better visualization. Spectra are measured at 30 °C (blue lines) and 90 °C (red lines). b) Spectra of transmission modulation depth spectra, calculated from data in a).

So far, we were discussing only two forms of VO_2, the dielectric and metallic one. But VO_2 can be also gradually tuned between those two forms. The gradual tuning arises mostly from the polycrystalline character of VO_2 films and structures [187]. To investigate this effect, we selected a representative array of nanocones (270 nm in diameter) and measured their transmission spectra while continuously changing the temperature (Figure 4.11a). To visualize the most pronounced modulation depth (Figure 4.10b), we extracted the transmission at 683 nm during the heating–cooling cycle as a function of temperature (Figure 4.11b). In the extracted graph, we can observe the characteristic gradual shift, with very narrow ($\approx 4\,°C$) hysteresis-like behavior with respect to the heating–cooling path. The narrow hysteresis curve results most probably from the identical size and shape of the measured nanocones that have a very similar transition temperature ($\approx 65\,°C$). However, it does not mean that optical properties of one nanocone change abruptly. Each nanocone might be composed of multiple grains, which lead to the gradual tuning already at the nanoscale [211]. Besides narrow hysteresis, we can also observe a remarkable 5.3 dB modulation depth of the transmission (from 0.15 to 0.5). Note that an unstructured 200 nm thin VO_2 film exhibited a 0.1 dB modulation depth at 683 nm, thus illustrating how strong the influence of nanostructuring is.
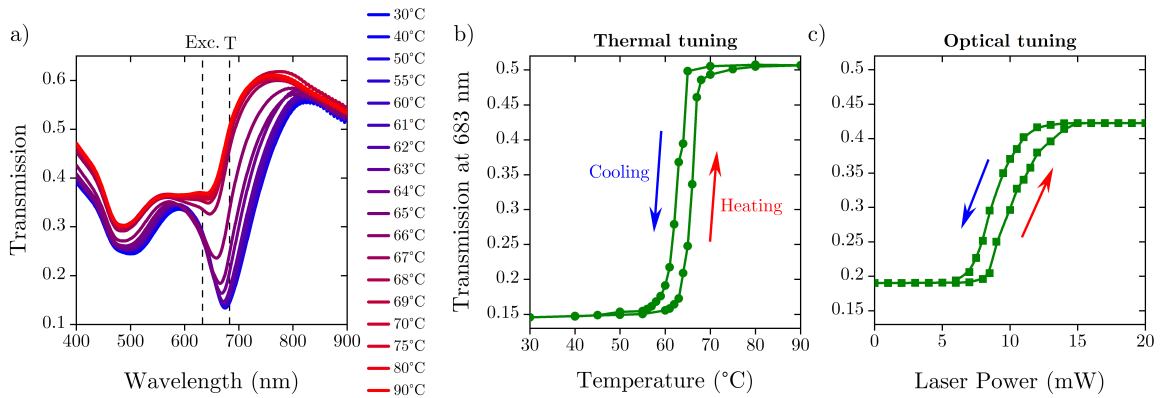
Figure 4.11: a) Transmission spectra of VO_2 nanocone arrays with 200 nm height, 1.5D spacing and 270 nm diameter. The transmission is measured at temperatures listed in the graph. The dashed vertical lines label the excitation (Exc.) and transmission measurement (T) wavelengths of b) and c) part. b) Hysteresis-like behavior of the measured transmission at 683 nm, as extracted from a). c) Hysteresis-like behavior of the transmission of the same array, measured at 683 nm upon continuous illumination by a continuous wave laser (633 nm) with gradually increasing power.

After proving and describing the gradual thermal tuning, we moved on to investigate optically-triggered VO$_2$ transition. The optical tuning of the same array of nanocones (270 nm in diameter) was provided by an additional 633 nm continuous wave laser, which illuminated the sample from the opposite side with respect to the white light source used for the transmission measurement. The reflected laser light was filtered out using a matching notch filter placed in front of the spectrometer. In Figure 4.11c we can see again the hysteresis-like behavior of the transmission at 683 nm, now induced by the increasing laser power. This transmission is however increased when VO$_2$ nanocones are in the dielectric form and decreased when they are in the metallic form. It can be caused by the notch filter and an inhomogeneous illumination of the heating laser. The inhomogeneous illumination, which results from the gaussian beam profile, is also responsible for the hysteresis curve widening. Despite these influences, observation of the optical tuning already proves a large potential of VO$_2$ in tunable metasurfaces, where the transmission phase and amplitude of each separate building block could be gradually tuned.

In summary, this chapter began by describing the optimization process of VO$_2$ thin film fabrication. We showed that 200 nm films evaporated and annealed for 10 min at 450 °C and under 15 sccm oxygen flow exhibit the largest FOM. As to obtain the FOM metric of the each optimized film is very time-consuming, we showed that for films thinner than 200 nm, even the transmission measured at 30 °C can be used as a quality factor. After obtaining the dielectric function from high-quality VO$_2$, we simulated pure VO$_2$ cylindrical building blocks in the VIS region. By varying different parameters of these blocks, we found that for a properly functional metasurface, pure VO$_2$ nanocylinders have to be at least 500 nm high. Despite their very low transmission, nanocylinders with this height and operating at 680 nm wavelength exhibited the best trade-off between the transmission phase (2π) and amplitude (10 %). Their huge advantage lied also in their phase modulation during the VO$_2$ transition, which reached values up to $3/2\pi$. To overcome the absorption problem, we suggested that pure VO$_2$ blocks could be more efficient in the NIR region. Trying to fabricate nanocylinders with such promising properties, we ended up with nanocones, or truncated nanocones of varying heights. While the phase of such structures was insufficient for a properly functional metasurface, we were able to use them to verify the validity of our simulations. We also showed that despite their phase insufficiency, nanocones with 200 nm height have exhibited dielectric Mie resonances which were subsequently exploited for a tunable transmission filter at the end of this chapter. Moreover, we proved the possibility of optical tuning on this filter, which has paved the way for optically controlled tunable metasurfaces.

Conclusion

This thesis was focused on examination and implementation of phase-changing VO_2 nanostructures into tunable metasurfaces operating in the VIS region. We started with a general description of metasurfaces, where we showed that metasurface nanostructures, often called building blocks, are responsible for altering the incident light wavefront. Based on the physics of the wavefront alteration via the building blocks, we divided metasurfaces into propagational and geometrical ones. After that, we presented the state-of-the-art metasurfaces, designed through forward or inverse approach. At the end of the first chapter we summarized various platforms that can be used to introduce tunability into metasurfaces.

The second chapter was focused on VO_2 as one of the most promising phase-change material that can be implemented into tunable metasurfaces. Its promising nature lies in low transition temperature ($67\,°C$), which can be replaced also by optical or electrical stimuli. As nanophotonic applications focus on optical properties, we decided to compare the VO_2 quality by the figure of merit (FOM), which was calculated from the complex refractive index of VO_2. Using the FOMs extracted from more than 80 different publications, we found the evidence against a common notion that high structural quality of VO_2 implies also low-loss optical properties, associated with large optical modulation in the VIS and NIR region. We concluded that VO_2 with large FOM and therefore large optical modulation can be obtained on any kind of substrate, using any kind of technique, but the proper optimization has to be carried out each time.

In the third chapter we briefly described the fabrication and characterization methods used within this thesis. For spectroscopic ellipsometry and coherence-controlled holographic microscopy, as characterization methods, we gave also a brief explanation of their underlying data analysis.

In the last chapter, we summarized all results concerning our VO_2 thin film optimization, fabrication of VO_2 building blocks, and performance of an optically tunable metasurface transmission filter. The VO_2 thin film was deposited by e-beam evaporation and subsequently annealed in vacuum furnace with controlled oxygen flow and temperature. After thorough optimization of annealing temperatures and oxygen flows

based on our defined FOM and transmission spectra as quality factors, we obtained the best annealing conditions for the 200 nm VO$_2$ film. The largest FOM was obtained for the film annealed for 10 min at 450 °C under 15 sccm oxygen flow. The absorption of our film was much smaller compared to values reported in most of the previous publications. Besides the optimized parameters we found that the fabrication is very sensitive to the substrate cleanliness, deposition rate and annealing conditions. Using the refractive index from the optimized film, we carried out numerous simulations in which we investigated influence of a cylindrical building block's height, spacing and wavelength on the transmitted phase and amplitude. We found that despite the resonant nature of the VO$_2$ nanocylinders, a functional tunable metasurface for the visible must be formed by high aspect ratio VO$_2$ blocks. We showed that nanocylinders with 500 nm height operating at 680 nm wavelength exhibited the best trade-off between the transmission phase (2π) and amplitude (10 %). Some of these nanocylinders also exhibited $3/2\pi$ phase modulation during the VO$_2$ transition, the value that was not reached by any tunable material in the visible, yet. We tried to fabricate nanocylinders with this height, but due to complications related to deposition and nanostructuring, we ended up with nanocones or truncated nanocones of varying heights. Their measured phase was not sufficient for a properly functional metasurface, but it served well enough to confirm our simulations. Although their influence in terms of propagation phase was insufficient, we showed that nanocones with 200 nm height exhibited dielectric Mie resonances which were subsequently exploited for a tunable transmission filter in the VIS region. The gradual tuning of such filter was presented both thermally and optically. With the gradual optical tuning we proved the possibility for nanoscale control of the optically tunable metasurface.

Despite the very promising results described above, we have to conclude that pure propagational VO$_2$ building blocks are not efficient enough for practical tunable metasurfaces in the VIS region, because of their inherent high absorption. We suggest that pure VO$_2$ building blocks should be rather used in the NIR region, where absorption is almost zero. For tunable metasurfaces in the VIS region, we suggest to replace pure VO$_2$ blocks by hybrid nanostructures in which VO$_2$ represents only a minor tunable component. Combining these suggestions with the verified optically tunable nature of VO$_2$ surely offers many opportunities for future research.

Bibliography

[1] Hecht, E. *Optics*. Pearson, Reading, 4th edn., 2002. ISBN 08-053-8566-5.

[2] Hsiao, H.-H., Chu, C. H., and Tsai, D. P. Fundamentals and Applications of Metasurfaces. *Small Methods*, 1 (4), **2017**, p. 20. DOI: 10.1002/smtd.201600064.

[3] Chokkattu, J. *A New Lens Technology Is Primed to Jump-Start Phone Cameras*. Wired, New York, 2021. Available at: https://www.wired.com/story/metalenz-smartphone-lens/.

[4] of Encyclopaedia, E. *Fresnel lens*. Encyclopedia Britannica, 2011. Available at: https://www.britannica.com/technology/Fresnel-lens.

[5] Fresnel, A. J. *Memoire sur la diffraction de la lumiere*. Annales de Chimie et de Physique, 1st edn., 1819.

[6] Wikipedia. *Fresnel lens*. San Francisco, California, 2006. Available at: https://en.wikipedia.org/wiki/Fresnel-lens.

[7] Taghizadeh, M., Blair, P., Layet, B., *et al.* Design and fabrication of diffractive optical elements. *Microelectronic Engineering*, 34 (3-4), **1997**, pp. 219–242. DOI: 10.1016/S0167-9317(97)00188-3.

[8] Chen, W. T., Zhu, A. Y., and Capasso, F. Flat optics with dispersion-engineered metasurfaces. *Nature Reviews Materials*, 5 (8), **2020**, pp. 604–620. DOI: 10.1038/s41578-020-0203-3.

[9] Meinzer, N., Barnes, W. L., and Hooper, I. R. Plasmonic meta-atoms and metasurfaces. *Nature Photonics*, 8 (12), **2014**, pp. 889–898. DOI: 10.1038/nphoton.2014.247.

[10] Ding, F., Yang, Y., Deshpande, R. A., and Bozhevolnyi, S. I. A review of gap-surface plasmon metasurfaces. *Nanophotonics*, 7 (6), **2018**, pp. 1129–1156. DOI: 10.1515/nanoph-2017-0125.

[11] Jahani, S. and Jacob, Z. All-dielectric metamaterials. *Nature Nanotechnology*, 11 (1), **2016**, pp. 23–36. DOI: 10.1038/nnano.2015.304.

[12] Kamali, S. M., Arbabi, E., Arbabi, A., and Faraon, A. A review of dielectric optical metasurfaces for wavefront control. *Nanophotonics*, 7 (6), **2018**, pp. 1041–1068. DOI: 10.1515/nanoph-2017-0129.

[13] Maier, S. A. *Plasmonics*. Springer, New York, 1 edn., 2007. ISBN 978-0-387-33150-8.

[14] Novotny, L. and Hecht, B. *Principles of nano-optics*. Cambridge University Press, Cambridge, 2nd ed edn., 2012. ISBN 978-1-107-00546-4.

[15] Pors, A. and Bozhevolnyi, S. I. Plasmonic metasurfaces for efficient phase control in reflection. *Optics Express*, 21 (22), **2013**, p. 14. DOI: 10.1364/OE.21.027438.

[16] Søndergaard, T., Jung, J., Bozhevolnyi, S. I., and Valle, G. D. Theoretical analysis of gold nano-strip gap plasmon resonators. *New Journal of Physics*, 10 (10), **2008**, p. 11. DOI: 10.1088/1367-2630/10/10/105008.

[17] Sun, S., Yang, K.-Y., Wang, C.-M., *et al.* High-Efficiency Broadband Anomalous Reflection by Gradient Meta-Surfaces. *Nano Letters*, 12 (12), **2012**, pp. 6223–6229. DOI: 10.1021/nl3032668.

[18] Kivshar, Y. All-dielectric meta-optics and non-linear nanophotonics. *National Science Review*, 5 (2), **2018**, pp. 144–158. DOI: 10.1093/nsr/nwy017.

[19] Staude, I., Miroshnichenko, A. E., Decker, M., *et al.* Tailoring Directional Scattering through Magnetic and Electric Resonances in Subwavelength Silicon Nanodisks. *ACS Nano*, 7 (9), **2013**, pp. 7824–7832. DOI: 10.1021/nn402736f.

[20] Zhang, T., Che, Y., Chen, K., *et al.* Anapole mediated giant photothermal nonlinearity in nanostructured silicon. *Nature Communications*, 11 (1), **2020**. DOI: 10.1038/s41467-020-16845-x.

[21] Gigli, C., Li, Q., Chavel, P., *et al.* Fundamental limitations of Huygens metasurfaces for optical beam shaping. *arXiv*, , **2020**. DOI: arXiv:2011.00232.

[22] Saleh, B. E. A. and Teich, M. C. *Fundamentals of photonics*. Wiley, Hoboken, 2nd ed edn., 2007. ISBN 978-0471358329.

[23] Chen, B. H., Wu, P. C., Su, V.-C., *et al.* GaN Metalens for Pixel-Level Full-Color Routing at Visible Light. *Nano Letters*, 17 (10), **2017**, pp. 6345–6352. DOI: 10.1021/acs.nanolett.7b03135.

[24] Mueller, B. J., Rubin, N. A., Devlin, R. C., *et al.* Metasurface Polarization Optics. *Physical Review Letters*, 118 (11), **2017**. DOI: 10.1103/PhysRevLett.118.113901.

[25] Cohen, E., Larocque, H., Bouchard, F., *et al.* Geometric phase from Aharonov–Bohm to Pancharatnam–Berry and beyond. *Nature Reviews Physics*, 1 (7), **2019**, pp. 437–449. DOI: 10.1038/s42254-019-0071-1.

[26] Kang, M., Feng, T., Wang, H.-T., and Li, J. Wave front engineering from an array of thin aperture antennas. *Optics Express*, 20 (14), **2012**. DOI: 10.1364/OE.20.015882.

[27] Lin, D., Fan, P., Hasman, E., and Brongersma, M. L. Dielectric gradient metasurface optical elements. *Science*, 345 (6194), **2014**, pp. 298–302. DOI: 10.1126/science.1253213.

[28] Nordmann, A. *Refraction - Huygens-Fresnel principle*. San Francisco, California, 2007. Available at: https://en.wikipedia.org/wiki/Huygens-Fresnel-principle.

[29] Zhou, Z., Li, J., Su, R., *et al.* Efficient Silicon Metasurfaces for Visible Light. *ACS Photonics*, 4 (3), **2017**, pp. 544–551. DOI: 10.1021/acsphotonics.6b00740.

[30] Liang, H., Lin, Q., Xie, X., *et al.* Ultrahigh Numerical Aperture Metalens at Visible Wavelengths. *Nano Letters*, 18 (7), **2018**, pp. 4460–4466. DOI: 10.1021/acs.nanolett.8b01570.

[31] Dong, Y., Xu, Z., Li, N., *et al.* Si metasurface half-wave plates demonstrated on a 12-inch CMOS platform. *Nanophotonics*, 9 (1), **2019**, pp. 149–157. DOI: 10.1515/nanoph-2019-0364.

[32] Chen, W. T., Khorasaninejad, M., Zhu, A. Y., *et al.* Generation of wavelength-independent subwavelength Bessel beams using metasurfaces. *Light Sci Appl*, 6 (5), **2017**, pp. e16259–e16259. DOI: 10.1038/lsa.2016.259.

[33] Shalaev, M. I., Sun, J., Tsukernik, A., *et al.* High-Efficiency All-Dielectric Metasurfaces for Ultracompact Beam Manipulation in Transmission Mode. *Nano Letters*, 15 (9), **2015**, pp. 6261–6266. DOI: 10.1021/acs.nanolett.5b02926.

[34] Zheng, G., Mühlenbernd, H., Kenney, M., *et al.* Metasurface holograms reaching 80% efficiency. *Nature Nanotechnology*, 10 (4), **2015**, pp. 308–312. DOI: 10.1038/nnano.2015.2.

[35] Ren, H., Briere, G., Fang, X., *et al.* Metasurface orbital angular momentum holography. *Nature Communications*, 10 (1), **2019**. DOI: 10.1038/s41467-019-11030-1.

[36] Li, J., Liu, C., Wu, T., *et al.* Efficient Polarization Beam Splitter Based on All-Dielectric Metasurface in Visible Region. *Nanoscale Research Letters*, 14 (1), **2019**. DOI: 10.1186/s11671-019-2867-4.

[37] Liu, Z., Zhu, D., Rodrigues, S. P., *et al.* Generative Model for the Inverse Design of Metasurfaces. *Nano Letters*, 18 (10), **2018**, pp. 6570–6576. DOI: 10.1021/acs.nanolett.8b03171.

[38] Shi, X., Qiu, T., Wang, J., *et al.* Metasurface inverse design using machine learning approaches. *Journal of Physics D: Applied Physics*, 53 (27), **2020**. DOI: 10.1088/1361-6463/ab8036.

[39] Lu, L., Joannopoulos, J. D., and Soljačić, M. Topological photonics. *Nature Photonics*, 8 (11), **2014**, pp. 821–829. DOI: 10.1038/nphoton.2014.248.

[40] Kruk, S., Hopkins, B., Kravchenko, I. I., *et al.* Invited Article. *APL Photonics*, 1 (3), **2016**. DOI: 10.1063/1.4949007.

[41] Wang, S., Wu, P. C., Su, V.-C., *et al.* Broadband achromatic optical metasurface devices. *Nature Communications*, 8 (1), **2017**. DOI: 10.1038/s41467-017-00166-7.

[42] Chen, W. T., Zhu, A. Y., Sisler, J., *et al.* Broadband Achromatic Metasurface-Refractive Optics. *Nano Letters*, 18 (12), **2018**, pp. 7801–7808. DOI: 10.1021/acs.nanolett.8b03567.

[43] Aieta, F., Genevet, P., Kats, M. A., *et al.* Aberration-Free Ultrathin Flat Lenses and Axicons at Telecom Wavelengths Based on Plasmonic Metasurfaces. *Nano Letters*, 12 (9), **2012**, pp. 4932–4936. DOI: 10.1021/nl302516v.

[44] Liang, H., Martins, A., Borges, B.-H. V., *et al.* High performance metalenses. *Optica*, 6 (12), **2019**. DOI: 10.1364/OPTICA.6.001461.

[45] Kang, L., Jenkins, R. P., and Werner, D. H. Recent Progress in Active Optical Metasurfaces. *Advanced Optical Materials*, 7 (14), **2019**. DOI: 10.1002/adom.201801813.

[46] Liu, F., Pitilakis, A., Mirmoosa, M. S., *et al.* Programmable Metasurfaces. *2018 IEEE International Symposium on Circuits and Systems (ISCAS)*, , **2018**, pp. 1–5. DOI: 10.1109/ISCAS.2018.8351817.

[47] Rovenská, K. *Dielektrické metapovrchy jako moderní optické prvky.* Diplomová práce, VUT Brno, Brno, 2020.

[48] Rovenska, K. *Fabrication and optimization of dielectric metalenses.* Brno, 2020. Available at: http://surfaces.fme.vutbr.cz/laboratories/developed-instruments/focusing-lens-as-a-dielectric-metasurface/.

[49] Nemati, A., Wang, Q., Hong, M., and Teng, J. Tunable and reconfigurable metasurfaces and metadevices. *Opto-Electronic Advances*, 1 (11), **2018**, pp. 180009–1.

[50] Kamali, S. M., Arbabi, E., Arbabi, A., *et al.* Highly tunable elastic dielectric metasurface lenses. *Laser Photonics Review*, 10 (6), **2016**, pp. 1002–1008. DOI: 10.1002/lpor.201600144.

[51] Ho, C. P., Pitchappa, P., Lin, Y.-S., *et al.* Electrothermally actuated micro-electromechanical systems based omega-ring terahertz metamaterial with polarization dependent characteristics. *Applied Physics Letters*, 104 (16), **2014**, p. 5. DOI: 10.1063/1.4871999.

[52] Cui, T., Bai, B., and Sun, H. Tunable Metasurfaces Based on Active Materials. *Advanced Functional Materials*, 29 (10), **2019**. DOI: 10.1002/adfm.201806692.

[53] Ou, J.-Y., Plum, E., Zhang, J., and Zheludev, N. I. An electromechanically reconfigurable plasmonic metamaterial operating in the near-infrared. *Nature Nanotechnology*, 8 (4), **2013**, pp. 252–255. DOI: 10.1038/nnano.2013.25.

[54] Rahmani, M., Xu, L., Miroshnichenko, A. E., *et al.* Reversible Thermal Tuning of All-Dielectric Metasurfaces. *Advanced Functional Materials*, 27 (31), **2017**. DOI: 10.1002/adfm.201700580.

[55] Lewi, T., Evans, H. A., Butakov, N. A., and Schuller, J. A. Ultrawide Thermo-optic Tuning of PbTe Meta-Atoms. *Nano Letters*, 17 (6), **2017**, pp. 3940–3945. DOI: 10.1021/acs.nanolett.7b01529.

[56] Chen, H.-T., Padilla, W. J., Zide, J. M. O., *et al.* Active terahertz metamaterial devices. *Nature*, 444 (7119), **2006**, pp. 597–600. DOI: 10.1038/nature05343.

[57] Shcherbakov, M. R., Liu, S., Zubyuk, V. V., *et al.* Ultrafast all-optical tuning of direct-gap semiconductor metasurfaces. *Nature Communications*, 8 (1), **2017**. DOI: 10.1038/s41467-017-00019-3.

[58] Thyagarajan, K., Sokhoyan, R., Zornberg, L., and Atwater, H. A. Millivolt Modulation of Plasmonic Metasurface Optical Response via Ionic Conductance. *Advanced Materials*, 29 (31), **2017**. DOI: 10.1002/adma.201701044.

[59] Guo, P., Schaller, R. D., Ketterson, J. B., and Chang, R. P. H. Ultrafast switching of tunable infrared plasmons in indium tin oxide nanorod arrays with large absolute amplitude. *Nature Photonics*, 10 (4), **2016**, pp. 267–273. DOI: 10.1038/nphoton.2016.14.

[60] Lee, S. H., Choi, M., Kim, T.-T., *et al.* Switching terahertz waves with gate-controlled active graphene metamaterials. *Nature Materials*, 11 (11), **2012**, pp. 936–941. DOI: 10.1038/nmat3433.

[61] Liu, P. Q., Valmorra, F., Maissen, C., and Faist, J. Electrically tunable graphene anti-dot array terahertz plasmonic crystals exhibiting multi-band resonances. *Optica*, 2 (2), **2015**. DOI: 10.1364/OPTICA.2.000135.

[62] Bohn, J., Bucher, T., Chong, K. E., *et al.* Active Tuning of Spontaneous Emission by Mie-Resonant Dielectric Metasurfaces. *Nano Letters*, 18 (6), **2018**, pp. 3461–3465. DOI: 10.1021/acs.nanolett.8b00475.

[63] Sautter, J., Staude, I., Decker, M., *et al.* Active Tuning of All-Dielectric Metasurfaces. *ACS Nano*, 9 (4), **2015**, pp. 4308–4315. DOI: 10.1021/acsnano.5b00723.

[64] Komar, A., Paniagua-Domínguez, R., Miroshnichenko, A., *et al.* Dynamic Beam Switching by Liquid Crystal Tunable Dielectric Metasurfaces. *ACS Photonics*, 5 (5), **2018**, pp. 1742–1748. DOI: 10.1021/acsphotonics.7b01343.

[65] Li, S.-Q., Xu, X., Veetil, R. M., *et al.* Phase-only transmissive spatial light modulator based on tunable dielectric metasurface. *Science*, 364 (6445), **2019**, pp. 1087–1090. DOI: 10.1126/science.aaw6747.

[66] Wuttig, M., Bhaskaran, H., and Taubner, T. Phase-change materials for non-volatile photonic applications. *Nature Photonics*, 11 (8), **2017**, pp. 465–476. DOI: 10.1038/nphoton.2017.126.

[67] Silva, J. L. F. D., Walsh, A., Wei, S.-H., and Lee, H. Atomistic origins of the phase transition mechanism in Ge2Sb2Te5. *Journal of Applied Physics*, 106 (11), **2009**. DOI: 10.1063/1.3264883.

[68] Abdollahramezani, S., Hemmatyar, O., Taghinejad, H., *et al.* Tunable nanophotonics enabled by chalcogenide phase-change materials. *Nanophotonics*, 9 (5), **2020**, pp. 1189–1241. DOI: 10.1515/nanoph-2020-0039.

[69] Tittl, A., Michel, A.-K. U., Schäferling, M., *et al.* A Switchable Mid-Infrared Plasmonic Perfect Absorber with Multispectral Thermal Imaging Capability. *Advanced Materials*, 27 (31), **2015**, pp. 4597–4603. DOI: 10.1002/adma.201502023.

[70] Yin, X., Steinle, T., Huang, L., *et al.* Beam switching and bifocal zoom lensing using active plasmonic metasurfaces. *Light Sci. Appl.*, 6 (7), **2017**, pp. e17016–e17016. DOI: 10.1038/lsa.2017.16.

[71] Bai, W., Yang, P., Huang, J., *et al.* Near-infrared tunable metalens based on phase change material Ge2Sb2Te5. *Scientific Reports*, 9 (1), **2019**. DOI: 10.1038/s41598-019-41859-x.

[72] Ding, X., Kang, Q., Guo, K., and Guo, Z. Tunable GST metasurfaces for chromatic aberration compensation in the mid-infrared. *Optical Materials*, 109, **2020**. DOI: 10.1016/j.optmat.2020.110284.

[73] de Galarreta, C. R., Sinev, I., Alexeev, A. M., *et al.* Reconfigurable multilevel control of hybrid all-dielectric phase-change metasurfaces. *Optica*, 7 (5), **2020**. DOI: 10.1364/OPTICA.384138.

[74] Leitis, A., Heßler, A., Wahl, S., *et al.* All-Dielectric Programmable Huygens' Metasurfaces. *Advanced Functional Materials*, 30 (19), **2020**. DOI: 10.1002/adfm.201910259.

[75] Delaney, M., Zeimpekis, I., Lawson, D., *et al.* A New Family of Ultralow Loss Reversible Phase-Change Materials for Photonic Integrated Circuits. *Advanced Functional Materials*, 30 (36), **2020**. DOI: 10.1002/adfm.202002447.

[76] Gutiérrez, Y., Brown, A. S., Moreno, F., and Losurdo, M. Plasmonics beyond noble metals. *Journal of Applied Physics*, 128 (8), **2020**. DOI: 10.1063/5.0020752.

[77] Dong, W., Liu, H., Behera, J. K., *et al.* Wide Bandgap Phase Change Material Tuned Visible Photonics. *Advanced Functional Materials*, 29 (6), **2019**. DOI: 10.1002/adfm.201806181.

[78] Morosan, E., Natelson, D., Nevidomskyy, A. H., and Si, Q. Strongly Correlated Materials. *Advanced Materials*, 24 (36), **2012**, pp. 4896–4923. DOI: 10.1002/adma.201202018.

[79] Lysenko, S., Vikhnin, V., Rúa, A., *et al.* Critical behavior and size effects in light-induced transition of nanostructured VO₂ films. *Physical Review B*, 82 (20), **2010**. DOI: 10.1103/PhysRevB.82.205425.

[80] Ramirez-Rincon, J. A., Gomez-Heredia, C. L., Corvisier, A., *et al.* Thermal hysteresis measurement of the VO₂ dielectric function for its metal-insulator transition by visible-IR ellipsometry. *Journal of Applied Physics*, 124 (19), **2018**. DOI: 10.1063/1.5049747.

[81] Kirilenko, V. V., Zhigarnovskiĭ, B. M., Beĭrakhov, A. G., *et al.* Synthesizing film-forming materials from vanadium oxides and investigating the possibilities of producing optical coatings based on them. *Journal of Optical Technology*, 77 (9), **2010**. DOI: 10.1364/JOT.77.000582.

[82] Morin, F. J. Oxides Which Show a Metal-to-Insulator Transition at the Neel Temperature. *Physical Review Letters*, 3 (1), **1959**, pp. 34–36. DOI: 10.1103/PhysRevLett.3.34.

[83] Cueff, S., John, J., Zhang, Z., *et al.* VO 2 nanophotonics. *APL Photonics*, 5 (11), **2020**. DOI: 10.1063/5.0028093.

[84] Imada, M., Fujimori, A., and Tokura, Y. Metal-insulator transitions. *Reviews of Modern Physics*, 70 (4), **1998**, pp. 1039–1263. DOI: 10.1103/RevModPhys.70.1039.

[85] Zhang, Y., Xiong, W., Chen, W., and Zheng, Y. Recent Progress on Vanadium Dioxide Nanostructures and Devices. *Nanomaterials*, 11 (2), **2021**. DOI: 10.3390/nano11020338.

[86] Biermann, S., Poteryaev, A., Lichtenstein, A. I., and Georges, A. Dynamical Singlets and Correlation-Assisted Peierls Transition in V O 2. *Physical Review Letters*, 94 (2), **2005**. DOI: 10.1103/PhysRevLett.94.026404.

[87] Eyert, V. The metal-insulator transitions of VO2: A band theoretical approach. *Ann. Phys.*, 11 (9), **2002**, p. 650 – 702. DOI: https://doi.org/10.1002/1521-3889(200210)11:9<650::AID-ANDP650>3.0.CO;2-K.

[88] Wentzcovitch, R. M., Schulz, W. W., and Allen, P. B. VO₂. *Physical Review Letters*, 72 (21), **1994**, pp. 3389–3392. DOI: 10.1103/PhysRevLett.72.3389.

[89] Chen, S.-C., Yuan, H.-K., Zhai, Z.-H., *et al.* All optically driven memory device for terahertz waves. *Optics Letters*, 45 (1), **2020**. DOI: 10.1364/OL.384740.

[90] Markov, P., Marvel, R. E., Conley, H. J., *et al.* Optically Monitored Electrical Switching in VO 2. *ACS Photonics*, 2 (8), **2015**, pp. 1175–1182. DOI: 10.1021/acsphotonics.5b00244.

[91] Thompson, Z. J., Stickel, A., Jeong, Y.-G., *et al.* Terahertz-Triggered Phase Transition and Hysteresis Narrowing in a Nanoantenna Patterned Vanadium Dioxide Film. *Nano Letters*, 15 (9), **2015**, pp. 5893–5898. DOI: 10.1021/acs.nanolett.5b01970.

[92] Pashkin, A., Kübler, C., Ehrke, H., *et al.* Ultrafast insulator-metal phase transition in VO 2 studied by multiterahertz spectroscopy. *Physical Review B*, 83 (19), **2011**. DOI: 10.1103/PhysRevB.83.195120.

[93] Liu, K., Lee, S., Yang, S., *et al.* Recent progresses on physics and applications of vanadium dioxide. *Materials Today*, 21 (8), **2018**, pp. 875–896. DOI: 10.1016/j.mattod.2018.03.029.

[94] Lu, C., Lu, Q., Gao, M., and Lin, Y. Dynamic Manipulation of THz Waves Enabled by Phase-Transition VO2 Thin Film. *Nanomaterials*, 11 (1), **2021**. DOI: 10.3390/nano11010114.

[95] Jian, J., Zhang, W., Jacob, C., *et al.* Roles of grain boundaries on the semiconductor to metal phase transition of VO 2 thin films. *Applied Physics Letters*, 107 (10), **2015**. DOI: 10.1063/1.4930831.

[96] Voloshenko, I., Gompf, B., Berrier, A., *et al.* Interplay between electronic and structural transitions in VO 2 revealed by ellipsometry. *J. Vac. Sci. Technol. B*, 37 (6), **2019**, pp. 061202–1–7. DOI: 10.1116/1.5121903.

[97] Lee, D., Lee, J., Song, K., *et al.* Sharpened VO 2 Phase Transition via Controlled Release of Epitaxial Strain. *Nano Letters*, 17 (9), **2017**, pp. 5614–5619. DOI: 10.1021/acs.nanolett.7b02482.

[98] Shvets, P., Dikaya, O., Maksimova, K., and Goikhman, A. A review of Raman spectroscopy of vanadium oxides. *Journal of Raman Spectroscopy*, 50 (8), **2019**, pp. 1226–1244. DOI: 10.1002/jrs.5616.

[99] Cakir, M. C., Kocer, H., Durna, Y., *et al.* Unveiling the optical parameters of vanadium dioxide in the phase transition region. *RSC Advances*, 10 (50), **2020**, pp. 29945–29955. DOI: 10.1039/D0RA05890D.

[100] John, J., Gutierrez, Y., Zhang, Z., *et al.* Multipolar Resonances with Designer Tunability Using VO$_2$ Phase-Change Materials. *Physical Review Applied*, 13 (4), **2020**. DOI: 10.1103/PhysRevApplied.13.044053.

[101] Donev, E. U., Hart, F. X., Nkurunziza, B. I., *et al.* Parametric study of optical transmission through plasmonic hole arrays modulated by the phase transition of vanadium dioxide. *OSA Continuum*, 3 (8), **2020**. DOI: 10.1364/OSAC.390879.

[102] Madaras, S. E., Creeden, J. A., Lahneman, D. J., *et al.* Dynamics of the blue pump-induced ultrafast insulator-to-metal transition and relaxation in VO$_2$ /TiO 2 and VO$_2$ /TiO 2. *Optical Materials Express*, 10 (6), **2020**. DOI: 10.1364/OME.394653.

[103] Howes, A., Zhu, Z., Curie, D., *et al.* Optical Limiting Based on Huygens' Metasurfaces. *Nano Letters*, 20 (6), **2020**, pp. 4638–4644. DOI: 10.1021/acs.nanolett.0c01574.

[104] Dai, K., Lian, J., Miller, M. J., *et al.* Optical properties of VO$_2$ thin films deposited on different glass substrates. *Optical Materials Express*, 9 (2), **2019**. DOI: 10.1364/OME.9.000663.

[105] Nagasaki, Y., Kohno, T., Bando, K., *et al.* Adaptive printing using VO$_2$ optical antennas with subwavelength resolution. *Applied Physics Letters*, 115 (16), **2019**. DOI: 10.1063/1.5109460.

[106] Wan, C., Zhang, Z., Woolf, D., *et al.* On the Optical Properties of Thin-Film Vanadium Dioxide from the Visible to the Far Infrared. *Annalen der Physik*, 531 (10), **2019**. DOI: 10.1002/andp.201900188.

[107] Houska, J., Kolenaty, D., Vlcek, J., and Cerstvy, R. Properties of thermochromic VO$_2$ films prepared by HiPIMS onto unbiased amorphous glass substrates at a low temperature of 300 °C. *Thin Solid Films*, 660, **2018**, pp. 463–470. DOI: 10.1016/j.tsf.2018.06.057.

[108] Fan, L., Wang, X., Wang, F., *et al.* Revealing the role of oxygen vacancies on the phase transition of VO$_2$ film from the optical-constant measurements. *RSC Advances*, 8 (34), **2018**, pp. 19151–19156. DOI: 10.1039/C8RA03292K.

[109] Uslu, M. E., Misirlioglu, I. B., and Sendur, K. Selective IR response of highly textured phase change VO$_2$ nanostructures obtained via oxidation of electron beam deposited metallic V films. *Optical Materials Express*, 8 (8), **2018**. DOI: 10.1364/OME.8.002035.

[110] Kim, S.-J., Choi, S., Sung, J., *et al.* Thickness and temperature dependency of variation of dielectric functions of phase-change VO$_2$ film. *2018 23rd Opto-Electronics and Communications Conference (OECC)*, , **2018**, pp. 1–2. DOI: 10.1109/OECC.2018.8729867.

[111] Wan, C., Horak, E. H., King, J., *et al.* Limiting Optical Diodes Enabled by the Phase Transition of Vanadium Dioxide. *ACS Photonics*, 5 (7), **2017**, pp. 2688–2692. DOI: 10.1021/acsphotonics.8b00313.

[112] Zhang, Z., Zuo, F., Wan, C., *et al.* Evolution of Metallicity in Vanadium Dioxide by Creation of Oxygen Vacancies. *Physical Review Applied*, 7 (3), **2017**. DOI: 10.1103/PhysRevApplied.7.034008.

[113] Currie, M., Mastro, M. A., and Wheeler, V. D. Characterizing the tunable refractive index of vanadium dioxide. *Optical Materials Express*, 7 (5), **2017**. DOI: 10.1364/OME.7.001697.

[114] Zhu, Z., Evans, P. G., Haglund, R. F., and Valentine, J. G. Dynamically Reconfigurable Metadevice Employing Nanostructured Phase-Change Materials. *Nano Letters*, 17 (8), **2017**, pp. 4881–4885. DOI: 10.1021/acs.nanolett.7b01767.

[115] Rajeswaran, B., Pradhan, J. K., Ramakrishna, S. A., and Umarji, A. M. Thermochromic VO$_2$ thin films on ITO-coated glass substrates for broadband high absorption at infra-red frequencies. *Journal of Applied Physics*, 122 (16), **2017**. DOI: 10.1063/1.5008730.

[116] Sun, J. and Pribil, G. K. Analyzing optical properties of thin vanadium oxide films through semiconductor-to-metal phase transition using spectroscopic ellipsometry. *Applied Surface Science*, 421, **2017**, pp. 819–823. DOI: 10.1016/j.apsusc.2016.09.125.

[117] Houska, J., Kolenaty, D., Rezek, J., and Vlcek, J. Characterization of thermochromic VO$_2$ (prepared at 250 °C) in a wide temperature range by spectroscopic ellipsometry. *Applied Surface Science*, 421, **2017**, pp. 529–534. DOI: 10.1016/j.apsusc.2016.10.084.

[118] Butakov, N. A., Valmianski, I., Lewi, T., *et al.* Switchable Plasmonic–Dielectric Resonators with Metal–Insulator Transitions. *ACS Photonics*, 5 (2), **2017**, pp. 371–377. DOI: 10.1021/acsphotonics.7b00334.

[119] Gaskell, J. M., Afzaal, M., Sheel, D. W., *et al.* Optimised atmospheric pressure CVD of monoclinic VO$_2$ thin films with picosecond phase

transition. *Surface and Coatings Technology*, 287, **2016**, pp. 160–165. DOI: 10.1016/j.surfcoat.2015.12.090.

[120] Huang, T., Yang, L., Qin, J., *et al.* Study of the phase evolution, metal-insulator transition, and optical properties of vanadium oxide thin films. *Optical Materials Express*, 6 (11), **2016**. DOI: 10.1364/OME.6.003609.

[121] Pan-Pan, W., Yu-Zhi, Z., Ming-Dong, P., *et al.* Spectroscopic ellipsometry analysis of vanadium oxide film in Vis-NIR and NIR-MIR. *Acta Physica Sinica*, 65 (12), **2016**. DOI: 10.7498/aps.65.127201.

[122] Cueff, S., Li, D., Zhou, Y., *et al.* Dynamic control of light emission faster than the lifetime limit using VO$_2$ phase-change. *Nature Communications*, 6 (1), **2015**. DOI: 10.1038/ncomms9636.

[123] Zhang, P., Jiang, K., Deng, Q., *et al.* Manipulations from oxygen partial pressure on the higher energy electronic transition and dielectric function of VO$_2$ films during a metal–insulator transition process. *Journal of Materials Chemistry C*, 3 (19), **2015**, pp. 5033–5040. DOI: 10.1039/C5TC00002E.

[124] Shibuya, K. and Sawa, A. Optimization of conditions for growth of vanadium dioxide thin films on silicon by pulsed-laser deposition. *AIP Advances*, 5 (10), **2015**. DOI: 10.1063/1.4934226.

[125] Seal, K., Sharoni, A., Messman, J. M., *et al.* Resolving transitions in the mesoscale domain configuration in VO$_2$ using laser speckle pattern analysis. *Scientific Reports*, 4 (1), **2015**. DOI: 10.1038/srep06259.

[126] Son, T., Zongo, K., Ba, C., *et al.* Pure optical phase control with vanadium dioxide thin films. *Optics Communications*, 320, **2014**, pp. 151–155. DOI: 10.1016/j.optcom.2014.01.037.

[127] Li, S.-Y., Niklasson, G. A., and Granqvist, C. G. Thermochromic undoped and Mg-doped VO$_2$ thin films and nanoparticles. *Journal of Applied Physics*, 115 (5), **2014**. DOI: 10.1063/1.4862930.

[128] Wei, Y., Ji-Ran, L., Jian, L., and Yang, J. Abnormal variation of optical properties of vanadium oxide thin film at semiconductor-metal transition. *Acta Physica Sinica*, 63 (10), **2014**. DOI: 10.7498/aps.63.107104.

[129] Krishnamoorthy, H. N. S., Zhou, Y., Ramanathan, S., *et al.* Tunable hyperbolic metamaterials utilizing phase change heterostructures. *Applied Physics Letters*, 104 (12), **2014**. DOI: 10.1063/1.4869297.

[130] Paik, T., Hong, S.-H., Gaulding, E. A., *et al.* Solution-Processed Phase-Change VO$_2$ Metamaterials from Colloidal Vanadium Oxide (VO x) Nanocrystals. *ACS Nano*, 8 (1), **2013**, pp. 797–806. DOI: 10.1021/nn4054446.

[131] Nazari, M., Zhao, Y., Kuryatkov, V. V., *et al.* Temperature dependence of the optical properties of VO$_2$ deposited on sapphire with different orientations. *Physical Review B*, 87 (3), **2013**. DOI: 10.1103/PhysRevB.87.035142.

[132] Bonora, S., Beydaghyan, G., Haché, A., and Ashrit, P. V. Mid-IR laser beam quality measurement through vanadium dioxide optical switching. *Optics Letters*, 38 (9), **2013**. DOI: 10.1364/OL.38.001554.

[133] Park, J.-B., Lee, I.-M., Lee, S.-Y., *et al.* Tunable subwavelength hot spot of dipole nanostructure based on VO$_2$ phase transition. *Optics Express*, 21 (13), **2013**. DOI: 10.1364/OE.21.015205.

[134] Luo, Y. Y., Zhu, L. Q., Zhang, Y. X., *et al.* Optimization of microstructure and optical properties of VO$_2$ thin film prepared by reactive sputtering. *Journal of Applied Physics*, 113 (18), **2013**. DOI: 10.1063/1.4803840.

[135] Li, S.-Y., Namura, K., Suzuki, M., *et al.* Thermochromic VO$_2$ nanorods made by sputter deposition. *Journal of Applied Physics*, 114 (3), **2013**. DOI: 10.1063/1.4813876.

[136] Joushaghani, A., Kruger, B. A., Paradis, S., *et al.* Sub-volt broadband hybrid plasmonic-vanadium dioxide switches. *Applied Physics Letters*, 102 (6), **2013**. DOI: 10.1063/1.4790834.

[137] Ba, C., Bah, S. T., D'Auteuil, M., *et al.* Fabrication of High-Quality VO$_2$ Thin Films by Ion-Assisted Dual ac Magnetron Sputtering. *ACS Appl. Mater. Interfaces*, 5 (23), **2013**, pp. 12520–12525. DOI: 10.1021/am403807u.

[138] Podraza, N. J., Gauntt, B. D., Motyka, M. A., *et al.* Electrical and optical properties of sputtered amorphous vanadium oxide thin films. *Journal of Applied Physics*, 111 (7), **2012**. DOI: 10.1063/1.3702451.

[139] Benkahoul, M., Chaker, M., Margot, J., *et al.* Thermochromic VO$_2$ film deposited on Al with tunable thermal emissivity for space applications. *Solar Energy Materials and Solar Cells*, 95 (12), **2011**, pp. 3504–3508. DOI: 10.1016/j.solmat.2011.08.014.

[140] van Zwol, P. J., Joulain, K., Ben-Abdallah, P., and Chevrier, J. Phonon polaritons enhance near-field thermal transfer across the phase transition of VO$_2$. *Physical Review B*, 84 (16), **2011**. DOI: 10.1103/PhysRevB.84.161413.

[141] Kana, J. K., Ndjaka, J., Vignaud, G., *et al.* Thermally tunable optical constants of vanadium dioxide thin films measured by spectroscopic ellipsometry. *Optics Communications*, 284 (3), **2011**, pp. 807–812. DOI: 10.1016/j.optcom.2010.10.009.

[142] Li, W. W., Zhu, J. J., Xu, X. F., *et al.* Ultraviolet-infrared dielectric functions and electronic band structures of monoclinic VO$_2$ nanocrystalline film. *Journal of Applied Physics*, 110 (1), **2011**. DOI: 10.1063/1.3601357.

[143] Li, W., Yu, Q., and Chu, J. H. Intrinsic evolutions of optical functions, band gap, and higher-energy electronic transitions in VO$_2$ film near the metal-insulator transition region. *Applied Physics Letters*, 99 (24), **2011**. DOI: https://doi.org/10.1063/1.3665626.

[144] Kang, L., Gao, Y., Luo, H., *et al.* Nanoporous Thermochromic VO$_2$ Films with Low Optical Constants, Enhanced Luminous Transmittance and Thermochromic Properties. *ACS Appl. Mater. Interfaces*, 3 (2), **2011**, pp. 135–138. DOI: 10.1021/am1011172.

[145] Briggs, R. M., Pryce, I. M., and Atwater, H. A. Compact silicon photonic waveguide modulator based on the vanadium dioxide metal-insulator phase transition. *Optics Express*, 18 (11), **2010**. DOI: 10.1364/OE.18.011192.

[146] Liu, G.-H., Deng, X.-Y., and Wen, R. Electronic and optical properties of monoclinic and rutile vanadium dioxide. *Journal of Materials Science*, 45 (12), **2010**, pp. 3270–3275. DOI: 10.1007/s10853-010-4338-2.

[147] Gentle, A. R., Smith, G. B., Lakhtakia, A., *et al.* Frequency and percolation dependence of the observed phase transition in nanostructured and doped VO$_2$ thin films. *Proc. SPIE: Nanostructured Thin Films*, 7041 (70410J), **2008**. DOI: 10.1117/12.792207.

[148] Mlyuka, N. R., Niklasson, G. A., and Granqvist, C. G. Thermochromic VO$_2$ -based multilayer films with enhanced luminous transmittance and solar modulation. *Physica status solidi (a)*, 206 (9), **2009**, pp. 2155–2160. DOI: 10.1002/pssa.200881798.

[149] Dicken, M. J., Aydin, K., Pryce, I. M., *et al.* Frequency tunable near-infrared metamaterials based on VO$_2$ phase transition. *Optics Express*, 17 (20), **2009**. DOI: 10.1364/OE.17.018330.

[150] Lappalainen, J., Heinilehto, S., Jantunen, H., and Lantto, V. Electrical and optical properties of metal-insulator-transition VO$_2$ thin films. *Journal of Electroceramics*, 22 (1-3), **2009**, pp. 73–77. DOI: 10.1007/s10832-008-9433-2.

[151] Kakiuchida, H., Jin, P., and Tazawa, M. Control of thermochromic spectrum in vanadium dioxide by amorphous silicon suboxide layer. *Solar Energy Materials and Solar Cells*, 92 (10), **2008**, pp. 1279–1284. DOI: 10.1016/j.solmat.2008.04.025.

[152] Mossanek, R. J. O. and Abbate, M. Optical response of metallic and insulating VO$_2$ calculated with the LDA approach. *Journal of Physics: Condensed Matter*, 19 (34), **2007**. DOI: 10.1088/0953-8984/19/34/346225.

[153] Kakiuchida, H., Jin, P., Nakao, S., and Tazawa, M. Optical Properties of Vanadium Dioxide Film during Semiconductive–Metallic Phase Transition. *Japanese Journal of Applied Physics*, 46 (No. 5), **2007**, pp. L113–L116. DOI: 10.1143/JJAP.46.L113.

[154] Kakiuchida, H., Jin, P., Okada, M., and Tazawa, M. Optical Characterization of Titanium–Vanadium Oxide Films. *Japanese Journal of Applied Physics*, 46 (2), **2007**, pp. 621–626. DOI: 10.1143/JJAP.46.621.

[155] Xu, G., Chen, Y., Tazawa, M., and Jin, P. Surface Plasmon Resonance of Silver Nanoparticles on Vanadium Dioxide. *The Journal of Physical Chemistry B*, 110 (5), **2006**, pp. 2051–2056. DOI: 10.1021/jp055744j.

[156] Xiao, D., Kim, K. W., and Zavada, J. M. Electrically programmable photonic crystal slab based on the metal-insulator transition in VO$_2$. *Journal of Applied Physics*, 97 (10), **2005**. DOI: 10.1063/1.1898435.

[157] Xu, G., Chen, Y., Tazawa, M., and Jin, P. Influence of dielectric properties of a substrate upon plasmon resonance spectrum of supported Ag nanoparticles. *Applied Physics Letters*, 88 (4), **2006**. DOI: 10.1063/1.2167827.

[158] Guinneton, F., Sauques, L., Valmalette, J.-C., *et al.* Optimized infrared switching properties in thermochromic vanadium dioxide thin films. *Thin Solid Films*, 446 (2), **2004**, pp. 287–295. DOI: 10.1016/j.tsf.2003.09.062.

[159] Garry, G., Durand, O., and Lordereau, A. Structural, electrical and optical properties of pulsed laser deposited VO$_2$ thin films on R- and C-sapphire planes. *Thin Solid Films*, 453-454, **2004**, pp. 427–430. DOI: 10.1016/j.tsf.2003.11.118.

[160] Xu, G., Jin, P., Tazawa, M., and Yoshimura, K. Tailoring of Luminous Transmittance upon Switching for Thermochromic VO$_2$ Films by Thickness Control. *Japanese Journal of Applied Physics*, 43 (1), **2004**, pp. 186–187. DOI: 10.1143/JJAP.43.186.

[161] Petit, C., Frigerio, J. M., Amra, C., and Macleod, H. A. Optical properties of VO$_2$ thin films in their dielectric and metallic states. *SPIE*, 1 (3738), **1999**, pp. 102–109. DOI: 10.1117/12.360070.

[162] Nagashima, M. and Wada, H. Near infrared optical properties of laser ablated VO$_2$ thin films by ellipsometry. *Thin Solid Films*, 312 (1-2), **1998**, pp. 61–65. DOI: 10.1016/S0040-6090(97)00360-X.

[163] Tazawa, M., Jin, P., and Tanemura, S. Optical constants of V$_{1-x}$W$_x$O$_2$ films. *Applied Optics*, 37 (10), **1998**. DOI: 10.1364/AO.37.001858.

[164] Thomas, M. S., DeNatale, J. F., and Hood, P. J. High-Temperature Optical Properties of Thin-Film Vanadium Oxides – VO$_2$ and V$_2$O$_3$. *MRS Proceedings*, 479, **1997**. DOI: 10.1557/PROC-479-161.

[165] Abe, H., Terauchi, M., Tanaka, M., *et al.* Electron Energy-loss Spectroscopy Study of the Metal-insulator Transition in VO$_2$. *Japanese Journal of Applied Physics*, 36 (Part 1, No. 1A), **1997**, pp. 165–169. DOI: 10.1143/JJAP.36.165.

[166] Choi, H. S., Ahn, J. S., Jung, J. H., *et al.* Mid-infrared properties of a VO$_2$ film near the metal-insulator transition. *Physical Review B*, 54 (7), **1996**, pp. 4621–4628. DOI: 10.1103/PhysRevB.54.4621.

[167] Partlow, D. P., Gurkovich, S. R., Radford, K. C., and Denes, L. J. Switchable vanadium oxide films by a sol-gel process. *Journal of Applied Physics*, 70 (1), **1991**, pp. 443–452. DOI: 10.1063/1.350272.

[168] Chain, E. E. Optical properties of vanadium dioxide and vanadium pentoxide thin films. *Applied Optics*, 30 (19), **1991**. DOI: 10.1364/AO.30.002782.

[169] Case, F. C. Improved VO$_2$ thin films for infrared switching. *Applied Optics*, 30 (28), **1991**. DOI: 10.1364/AO.30.004119.

[170] Parker, J. C., Geiser, U. W., Lam, D. J., *et al.* Optical Properties of the Vanadium Oxides VO$_2$ and V$_2$O$_5$. *Journal of the American Ceramic Society*, 73 (11), **1990**, pp. 3206–3208. DOI: 10.1111/j.1151-2916.1990.tb06438.x.

[171] Case, F. C. Effects of low-energy low-flux ion bombardment on the properties of VO$_2$ thin films. *Journal of Vacuum Science & Technology A*, 7 (3), **1989**, pp. 1194–1198. DOI: 10.1116/1.576252.

[172] Chain, E. E. Effects of oxygen in ion-beam sputter deposition of vanadium oxide. *Journal of Vacuum Science & Technology A*, 5 (4), **1987**, pp. 1836–1839. DOI: 10.1116/1.574510.

[173] Case, F. C. Influence of ion beam parameters on the electrical and optical properties of ion-assisted reactively evaporated vanadium dioxide thin films. *Journal of Vacuum Science & Technology A*, 5 (4), **1987**, pp. 1762–1766. DOI: 10.1116/1.574534.

[174] Balberg, I. and Trokman, S. High-contrast optical storage in VO$_2$ films. *Journal of Applied Physics*, 46 (5), **1975**, pp. 2111–2119. DOI: 10.1063/1.321849.

[175] Gavini, A. and Kwan, C. C. Y. Optical Properties of Semiconducting VO$_2$ Films. *Physical Review B*, 5 (8), **1972**, pp. 3138–3143. DOI: 10.1103/PhysRevB.5.3138.

[176] Verleur, H. W., Barker, A. S., and Berglund, C. N. Optical Properties of VO$_2$ between 0.25 and 5 eV. *Physical Review*, 172 (3), **1968**, pp. 788–798. DOI: 10.1103/PhysRev.172.788.

[177] Fortier, J.-P., Baloukas, B., Zabeida, O., *et al.* Thermochromic VO$_2$ thin films deposited by HiPIMS. *Solar Energy Materials and Solar Cells*, 125, **2014**, pp. 291–296. DOI: 10.1016/j.solmat.2014.03.007.

[178] Liu, H., Wang, Z.-H., Li, L., *et al.* Vanadium dioxide-assisted broadband tunable terahertz metamaterial absorber. *Scientific Reports*, 9 (1), **2019**. DOI: 10.1038/s41598-019-42293-9.

[179] Ligmajer, F., Kejík, L., Tiwari, U., *et al.* Epitaxial VO 2 Nanostructures. *ACS Photonics*, 5 (7), **2017**, pp. 2561–2567. DOI: 10.1021/acsphotonics.7b01384.

[180] Muraoka, Y. and Hiroi, Z. Metal–insulator transition of VO$_2$ thin films grown on TiO2 (001) and (110) substrates. *Applied Physics Letters*, 80 (4), **2002**, pp. 583–585. DOI: 10.1063/1.1446215.

[181] Brassard, D., Fourmaux, S., Jean-Jacques, M., *et al.* Grain size effect on the semiconductor-metal phase transition characteristics of magnetron-sputtered VO2 thin films. *Applied Physics Letters*, 87 (5), **2005**. DOI: 10.1063/1.2001139.

[182] Jin, P., Yoshimura, K., and Tanemura, S. Dependence of microstructure and thermochromism on substrate temperature for sputter-deposited VO2 epitaxial films. *Journal of Vacuum Science & Technology A*, 15 (3), **1997**, pp. 1113–1117. DOI: 10.1116/1.580439.

[183] Nakano, M., Shibuya, K., Okuyama, D., *et al.* Collective bulk carrier delocalization driven by electrostatic surface charge accumulation. *Nature*, 487 (7408), **2012**, pp. 459–462. DOI: 10.1038/nature11296.

[184] Liu, C., Wang, Y., Tian, Z., and Mei, Y. Low-dimensional vanadium dioxide nanomaterials. *Journal of Physics: Materials*, 3 (3), **2020**. DOI: 10.1088/2515-7639/aba1d6.

[185] Vu, T. D., Chen, Z., Zeng, X., *et al.* Physical vapour deposition of vanadium dioxide for thermochromic smart window applications. *Journal of Materials Chemistry C*, 7 (8), **2019**, pp. 2121–2145. DOI: 10.1039/C8TC05014G.

[186] Earl, S. K., James, T. D., Davis, T. J., *et al.* Tunable optical antennas enabled by the phase transition in vanadium dioxide. *Optics Express*, 21 (22), **2013**. DOI: 10.1364/OE.21.027503.

[187] Appavoo, K. and Haglund, R. F. Detecting Nanoscale Size Dependence in VO 2 Phase Transition Using a Split-Ring Resonator Metamaterial. *Nano Letters*, 11 (3), **2011**, pp. 1025–1031. DOI: 10.1021/nl103842v.

[188] Lei, D. Y., Appavoo, K., Ligmajer, F., *et al.* Optically-Triggered Nanoscale Memory Effect in a Hybrid Plasmonic-Phase Changing Nanostructure. *ACS Photonics*, 2 (9), **2015**, pp. 1306–1313. DOI: 10.1021/acsphotonics.5b00249.

[189] Ferrara, D. W., Nag, J., MacQuarrie, E. R., *et al.* Plasmonic Probe of the Semiconductor to Metal Phase Transition in Vanadium Dioxide. *Nano Letters*, 13 (9), **2013**, pp. 4169–4175. DOI: 10.1021/nl401823r.

[190] Liu, L., Kang, L., Mayer, T. S., and Werner, D. H. Hybrid metamaterials for electrically triggered multifunctional control. *Nature Communications*, 7 (1), **2016**. DOI: 10.1038/ncomms13236.

[191] Earl, S. K., James, T. D., Gómez, D. E., *et al.* Switchable polarization rotation of visible light using a plasmonic metasurface. *APL Photonics*, 2 (1), **2017**. DOI: 10.1063/1.4968840.

[192] Kim, Y., Wu, P. C., Sokhoyan, R., *et al.* Phase Modulation with Electrically Tunable Vanadium Dioxide Phase-Change Metasurfaces. *Nano Letters*, 19 (6), **2019**, pp. 3961–3968. DOI: 10.1021/acs.nanolett.9b01246.

[193] Yang, J.-K. and Jeong, H.-S. Switchable Metasurface with VO2 Thin Film at Visible Light by Changing Temperature. *Photonics*, 8 (2), **2021**. DOI: 10.3390/photonics8020057.

[194] Lv, F., Xiao, Z., Lu, X., *et al.* Polarization Conversion and Absorption of Multifunctional All-dielectric Metamaterial Based on Vanadium Dioxide. *Plasmonics*, 16 (2), **2021**, pp. 567–574. DOI: 10.1007/s11468-020-01326-0.

[195] Takase, H. and Takahara, J. Switchable wavefront control using an all-dielectric metasurface mediated by VO 2. *Applied Physics Express*, 14 (3), **2021**. DOI: 10.35848/1882-0786/abdd13.

[196] Bashir, A., Awan, T. I., Tehseen, A., *et al.* Interfaces and surfaces. *Chemistry of Nanomaterials*, , **2020**, pp. 51–87. DOI: 10.1016/B978-0-12-818908-5.00003-2.

[197] Liška, J., Ligmajer, F., N., P. V. P., *et al.* Effect of deposition angle on fabrication of plasmonic gold nanocones and nanodiscs. *Microelectronic Engineering*, 228, **2020**. DOI: 10.1016/j.mee.2020.111326.

[198] Zhang, J. and Hoshino, K. *Molecular Sensors and Nanodevices.* Academic Press, 2nd edition edn., 2018. ISBN 9780128148624.

[199] Fujiwara, H. *Spectroscopic Ellipsometry.* John Wiley & Sons, Ltd, Hoboken, New Jersey, 1st ed edn., 2007. ISBN 9780470016084.

[200] Rollo, S., Rani, D., Olthuis, W., and García, C. P. Single step fabrication of Silicon resistors on SOI substrate used as Thermistors. *Scientific Reports*, 9 (1), **2019**. DOI: 10.1038/s41598-019-38753-x.

[201] Yue, W., Gao, S., Lee, S.-S., *et al.* Highly reflective subtractive color filters capitalizing on a silicon metasurface integrated with nanostructured aluminum mirrors. *Laser Photonics Rev.*, 11 (3), **2017**. DOI: 10.1002/lpor.201600285.

[202] Kepič, P. *Pole plazmonických nanostruktur tvořených materiály s fázovou přeměnou.* Bakalářská práce, VUT Brno, Brno, 2019.

[203] Manfrinato, V. R., Zhang, L., Su, D., *et al.* Resolution Limits of Electron-Beam Lithography toward the Atomic Scale. *Nano Letters*, 13 (4), **2013**, pp. 1555–1558. DOI: 10.1021/nl304715p.

[204] Slabý, T. *Koherencí řízený holografický mikroskop nové generace.* Dizertační práce, VUT Brno, Brno, 2014.

[205] Cuche, E., Bevilacqua, F., and Depeursinge, C. Digital holography for quantitative phase-contrast imaging. *Optics Letters*, 24 (5), **1999**. DOI: 10.1364/OL.24.000291.

[206] Kepič, P., Ligmajer, F., Hrtoň, M., *et al.* Optically Tunable Mie Resonance VO 2 Nanoantennas for Metasurfaces in the Visible. *ACS Photonics*, 8 (4), **2021**, pp. 1048–1057. DOI: 10.1021/acsphotonics.1c00222.

[207] Li, Z., Yu, S., and Zheng, G. Advances in exploiting the degrees of freedom in nanostructured metasurface design. *Nanophotonics*, 9 (12), **2020**, pp. 3699–3731. DOI: 10.1515/nanoph-2020-0127.

[208] Zhan, A., Colburn, S., Trivedi, R., *et al.* Low-Contrast Dielectric Metasurface Optics. *ACS Photonics*, 3 (2), **2016**, pp. 209–214. DOI: 10.1021/acsphotonics.5b00660.

[209] Babocký, J. *Tvorba plazmonických mikro a nanostruktur pomocí elektronové litografie.* Master's thesis, VUT Brno, 2012.

[210] Lawrence, M., Barton, D. R., Dixon, J., *et al.* High quality factor phase gradient metasurfaces. *Nature Nanotechnology*, 15 (11), **2020**, pp. 956–961. DOI: 10.1038/s41565-020-0754-x.

[211] Frenzel, A., Qazilbash, M. M., Brehm, M., *et al.* Inhomogeneous electronic state near the insulator-to-metal transition in the correlated oxide VO 2. *Physical Review B*, 80 (11), **2009**. DOI: 10.1103/PhysRevB.80.115115.